



TITLE:

An Ancient >200 m Cumulative Normal Faulting Displacement Along the Futagawa Fault Dextrally Ruptured During the 2016 Kumamoto, Japan, Earthquake Identified by a Multiborehole Drilling Program

AUTHOR(S):

Shibutani, Susumu; Lin, Weiren; Sado, Koichiro; Aizawa, Akihiro; Koike, Katsuaki

CITATION:

Shibutani, Susumu ...[et al]. An Ancient >200 m Cumulative Normal Faulting Displacement Along the Futagawa Fault Dextrally Ruptured During the 2016 Kumamoto, Japan, Earthquake Identified by a Multiborehole Drilling Program. Geochemistry, Geophys ...

ISSUE DATE:

2022-01

URL:

<http://hdl.handle.net/2433/267728>

RIGHT:

© 2022 The Authors.; This is an open access article under the terms of the Creative Commons Attribution-NonCommercial License, which permits use, distribution and reproduction in any medium, provided the original work is properly cited and is not used for commercial purposes.

Geochemistry, Geophysics, Geosystems®



RESEARCH ARTICLE

10.1029/2021GC009966

Key Points:

- Multiborehole drilling through the currently dextral Futagawa fault zone reveals >200 m of cumulative normal-sense displacement
- The switch from normal to dextral motion was probably due to termination of the Aso caldera-forming eruption sequence at ~87 ka
- Geological and geophysical data suggest the fault zone at ~461 m depth experienced dextral-sense slip during the 2016 Kumamoto earthquake

Correspondence to:

W. Lin,
lin@kumst.kyoto-u.ac.jp

Citation:

Shibutani, S., Lin, W., Sado, K., Aizawa, A., & Koike, K. (2022). An ancient >200 m cumulative normal faulting displacement along the Futagawa fault dextrally ruptured during the 2016 Kumamoto, Japan, earthquake identified by a multiborehole drilling program. *Geochemistry, Geophysics, Geosystems*, 23, e2021GC009966. <https://doi.org/10.1029/2021GC009966>

Received 14 JUN 2021

Accepted 9 JAN 2022

Author Contributions:

Conceptualization: Susumu Shibutani, Weiren Lin

Data curation: Susumu Shibutani, Koichiro Sado, Akihiro Aizawa

Formal analysis: Susumu Shibutani

Investigation: Susumu Shibutani, Koichiro Sado, Akihiro Aizawa

Methodology: Susumu Shibutani, Weiren Lin

Supervision: Weiren Lin, Katsuaki Koike

Visualization: Susumu Shibutani, Weiren Lin

Writing – original draft: Susumu Shibutani, Weiren Lin

An Ancient >200 m Cumulative Normal Faulting Displacement Along the Futagawa Fault Dextrally Ruptured During the 2016 Kumamoto, Japan, Earthquake Identified by a Multiborehole Drilling Program

Susumu Shibutani^{1,2} , Weiren Lin¹ , Koichiro Sado³, Akihiro Aizawa³, and Katsuaki Koike¹ 

¹Graduate School of Engineering, Kyoto University, Kyoto, Japan, ²Chi-ken Sogo Consultants Co., Ltd. (Shikoku Branch), Niihama, Japan, ³Chi-ken Sogo Consultants Co., Ltd. (Headquarters), Tokyo, Japan

Abstract The Mw 7.0 mainshock of the 2016 Kumamoto earthquake sequence was triggered by dextral rupture of the Futagawa fault within the Aso volcanic region, Southwestern Japan. To reproduce its faulting patterns and to reveal the geological and geophysical characteristics of the fault and surrounding lithological units, we report the results of a multiple-borehole drilling program penetrating the Futagawa fault zone. By combining core descriptions with geophysical logs, we identified >200 m of normal faulting displacement along the currently dextral strike-slip Futagawa fault. Considering previous kinematic and chronological studies of the fault, we interpret that the Futagawa fault dominantly slipped as a normal fault in a short period (~300–87 ka) before switching to its current transtensional (dominant strike-slip) regime ~87 ka caused by a local change in the stress field associated with the termination of the Aso caldera-forming eruptions. In the main borehole, three damage/slip zones were penetrated at depths of ~354, 461, and 576 m. The 461 damage zone was identified as ~45 m in vertical thickness and thicker than the other damage zones (~3–6 m vertically) and was characterized by high fracture density and the presence of strike-slip slickenlines. Depth profiles of physical properties revealed different patterns near the three damage zones; both the resistivity and the P-wave velocity showed stronger deterioration at the 461 damage zone than the others. Based on these geological and geophysical observations, we suggest that the 461 damage zone is the primary candidate for seismogenic faulting during the 2016 Kumamoto earthquake mainshock.

Plain Language Summary The Mw 7.0 mainshock of the 2016 Kumamoto earthquake sequence was caused by slipping along the Futagawa fault within the Aso volcanic region of Southwestern Japan. To investigate its faulting patterns, the geological structure and geophysical properties of the fault and surrounding units, we report the results of the Futagawa fault drilling project in which multiple boreholes were drilled through the fault zone. We found >200 m of normal faulting displacement along the currently strike-slip Futagawa fault. Taking previous studies together, we interpret that the Futagawa fault dominantly slipped as a normal fault in a short period (~300–87 kyr ago) before switching to its current strike-slip mode ~87 kyr ago caused by termination of the Aso caldera-forming eruption sequence. In the ~700 m-deep main borehole, three damage zones were identified. The second damage zone at ~461 m depth was more strongly damaged than the others. In addition, the physical properties revealed different change patterns near the three damage zones and showed strongest deterioration at the 461-m damage zone. Based on geological and geophysical observations, we suggest that this damage zone is the primary candidate that caused the 2016 Kumamoto earthquake mainshock.

1. Introduction

The Southwest Japan arc and Ryukyu arc are located on the subduction zone where the Philippine Sea plate subducts beneath the Eurasian plate (or the Amurian subplate) at the Nankai Trough and Ryukyu Trench, respectively (Kamata & Kodama, 1999; Figure 1a). The Philippine Sea plate subducted beneath Kyushu from ~6 Ma, and was rotated in the counterclockwise direction from north-northwest to west-northwest at ~2 Ma (e.g., Kamata & Kodama, 1999; Wu et al., 2016). Volcanism in central Kyushu related to subduction of the Philippine Sea plate began at ~5 Ma (Nakada & Kamata, 1991). At the junction of the two arcs, subduction of fluid-rich oceanic crust and sediments introduced large volumes of fluids into the Kyushu arc system, leading to voluminous volcanism and a locally extensional stress regime (Mahony et al., 2011). As a result, the Aso Volcano, one of the greatest

© 2022 The Authors.

This is an open access article under the terms of the [Creative Commons Attribution-NonCommercial License](https://creativecommons.org/licenses/by-nc/4.0/), which permits use, distribution and reproduction in any medium, provided the original work is properly cited and is not used for commercial purposes.

Writing – review & editing: Susumu Shibutani, Weiren Lin, Koichiro Sado, Akihiro Aizawa, Katsuaki Koike

volcanoes in the world, erupted mainly during $\sim 0.3\text{--}0.09$ Ma and formed a large caldera ~ 25 km in size in the north-south direction and ~ 18 km in the east-west direction (e.g., Mahony et al., 2011). In addition, the Beppu-Shimabara graben developed in central Kyushu, where this study area is located, and exhibits active faulting (e.g., Kamata & Kodama, 1999; Mahony et al., 2011; Figure 1b), which coincides with vigorous magmatic activity. The Oita-Kumamoto Tectonic Line (OKTE) exists on the southeastern margin of the graben and across the Aso caldera (Kusumoto, 2016). The Futagawa fault in the Aso volcanic region, the target of this study, composes a part of the OKTE. In addition, the Beppu-Shimabara graben consists of several smaller grabens, including the Kiyama-Kashima graben on the southeastern margin, where the Futagawa fault is partially situated (Figure 2a).

On 16 April 2016 (Japan Time), a Mw 7.0 earthquake (mainshock) occurred along the Futagawa fault in Kumamoto Prefecture, central Kyushu, southwestern Japan, following a Mw 6.2 foreshock ~ 28 hr after its occurrence (Toda et al., 2016). This Kumamoto earthquake mainshock occurred in the Aso volcanic region at the junction of the Southwest Japan arc and Ryukyu arc formed by Philippine Sea plate subduction. The earthquake rupture was limited to a zone of high seismic wave velocity and low Poisson's ratio in the upper crust but not surrounding or underlying zones of low velocity and high Poisson's ratio (Zhao et al., 2018). This structural feature suggests that strong structural and magmatic heterogeneities relating to active volcanoes and magmatic fluids exist in and around the source zone of the earthquake, which may affect seismogenesis (Zhao et al., 2018). Similarly, Moore et al. (2017) used the large stress perturbation incurred by the earthquake sequence to suggest that the earthquake illuminated distinct regions of low effective viscosity in the lower crust, notably beneath the Aso and Kuju volcanoes surrounded by large-scale variations in viscosity across the back-arc. In addition, the 2016 Kumamoto earthquake mainshock (Mw 7.0) coseismically and postseismically caused significant hydrochemical and hydrogeological changes, such as a groundwater helium anomaly, groundwater level drawdown, permeability changes, and long-term solute fluxes from active volcanic systems (Hosono et al., 2018, 2019, 2020; Sano et al., 2016). During the earthquake, surface ruptures that were approximately 28 km long appeared along the ENE-WSW-trending Futagawa fault zone on the western side of Aso Volcano (Figure 2a). Large dextral slip with a maximum displacement of 2.2 m was measured throughout the central section of the rupture zone along the Futagawa fault, which is nearly vertical near the surface and dips northwestward at depth (Shirahama et al., 2016; Yano & Matsubara, 2017). Moya et al. (2017) calculated the coseismic displacement along the Futagawa fault using a pair of digital surface models obtained from LiDAR data before and after the mainshock. This work revealed that a relative vertical displacement of ~ 1.4 m occurred gradually within an ~ 1.5 km range shown by a pair of blue brackets in Figure 2a around the surface rupture rather than a sudden change immediately across the surface rupture in the area of our research site, which is denoted as “Futagawa fault drilling project” (FFDP) in Figure 2a. This result indicated that the hanging wall (northwestern side of the surface rupture) subsided relatively. Therefore, the Futagawa fault exhibits a normal faulting component with dominant strike-slip (Moya et al., 2017; Shirahama et al., 2016). According to the Kobayashi et al. (2017) rupture model, the maximum coseismic slip displacement in strike-slip mode occurred at a depth range of $\sim 1\text{--}6$ km below the surface and attained >4 m. In addition, Toda et al. (2016) confirmed ~ 10 km-long segmented normal fault scarps, dipping to the northwest, along the previously mapped Idenokuchi fault, 1.2–2.0 km south of and subparallel to the Futagawa fault through field observations and offset measurements of surface rupture immediately after the Kumamoto earthquake mainshock (Figure 2a). Combining InSAR images with geodetic and seismic inversions of subsurface fault slip, they present a schematic structural model where oblique motion occurred on a northwest-dipping subsurface fault and the slip was partitioned at the surface into strike-slip on the Futagawa fault and dip-slip on the Idenokuchi fault (Toda et al., 2016). Yoshida (2017) analyzed focal mechanisms of the Kumamoto earthquake sequence (events of $4.0 \leq M_w \leq 7.0$ occurred between 14 April 2016 and 22 January 2017) and showed that almost all earthquakes that occurred along the Futagawa-Hinagu fault zone fall into two faulting regimes: The strike-slip faulting regime and the normal faulting regime with or without a minor strike-slip component. This suggests a current transtensional (dominant strike-slip) environment around the Futagawa fault.

The Futagawa fault was surveyed and first defined as a normal fault with a 70–100 m offset dipping north-northwest (Oohashi et al., 2020; Watanabe & Ono, 1969). However, this fault clearly ruptured in a dominantly strike-slip faulting regime during the mainshock of the 2016 Kumamoto earthquake (Shirahama et al., 2016). Because faulting mechanism and volcanism are known to be interrelated (e.g., Feuillet, 2013; Waite & Smith, 2002), we consider that the change in faulting pattern from dominantly normal faulting in the past to current/recent strike-slip faulting could be related to the tectonic environment in the Aso volcanic region in the subduction system. Therefore, we aim to discover any evidence that reveals ancient and recent rupturing patterns of the Futagawa

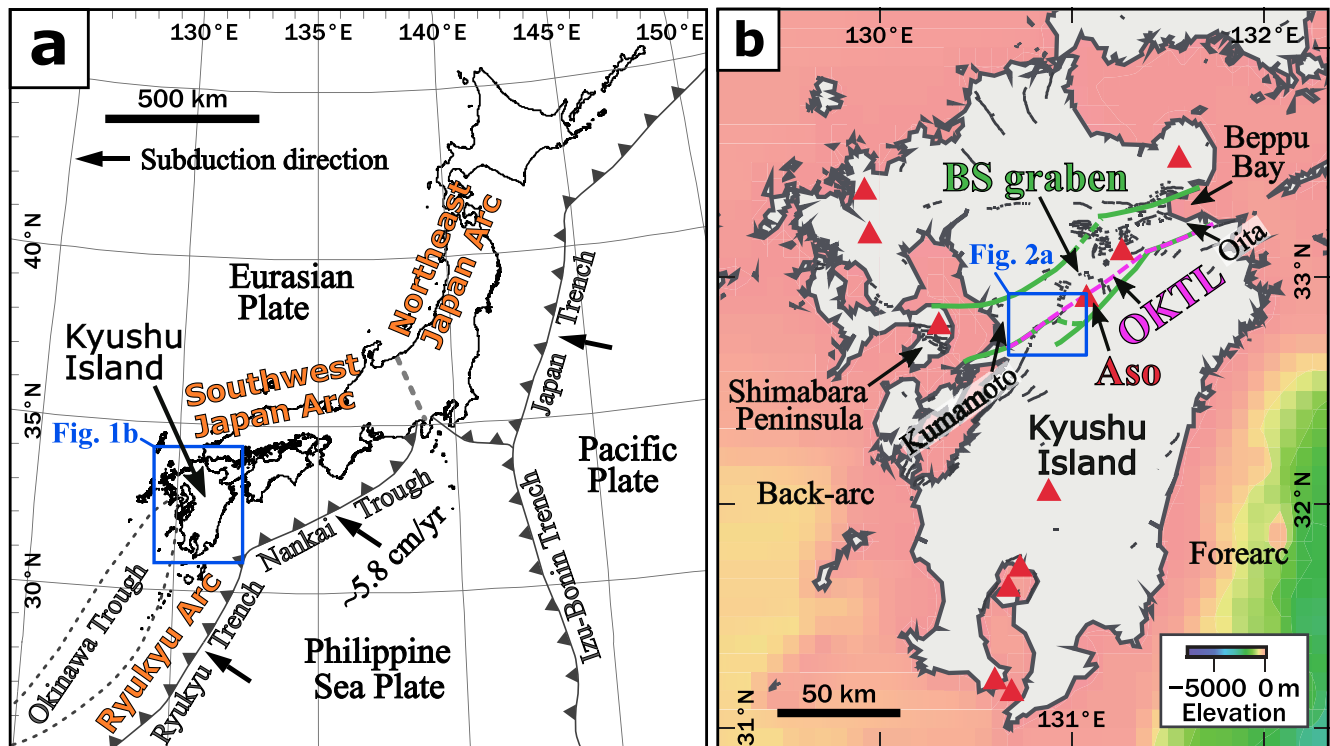


Figure 1. Tectonic framework around the Japanese Islands and Kyushu Island. Panels (a and b) were modified from Shirahama et al. (2016) and Mahony et al. (2011), respectively. (a) Location of the study area in Kyushu, southwest Japan. The blue square shows the area of map in panel (b). The Southwest Japan and Ryukyu arcs, Nankai Trough, Okinawa Trough, Ryukyu Trench and direction of plate subduction are from Kamata and Kodama (1999). Rate of ~ 5.8 cm/year indicates the relative convergence rate of the Philippine Sea plate from DeMets et al. (2010). (b) Detailed active tectonic setting in Kyushu. Red triangles indicate key volcanos. Oita-Kumamoto Tectonic Line (OKTL) is shown by dashed magenta line; Beppu-Shimabara (BS) graben is by green lines. OKTL and BS graben are from Kusumoto (2016). The blue square shows the area of Figure 2a.

fault through geological structures and physical properties around the fault. For this purpose, we describe the results of a multiborehole fault drilling program completed soon after the earthquake and discuss the effects of volcanism on fault activity.

A multiborehole fault drilling program can penetrate an active fault at different locations to reveal both ancient and current displacements in the fault zone and provide geological and geophysical data and drill core samples in the fault zone and host rocks. Scientific fault drilling campaigns have been conducted in many countries to clarify the mechanisms of fault activity that cause earthquakes. For example, in fault drilling research, the Nojima fault scientific drilling program (Nojima Fault Zone Probe) in Japan (the 1995 Mw 7.2 Kobe earthquake), the Taiwan Chelungpu-Fault Drilling Project in Taiwan (the 1999 Mw 7.6 Chi-Chi earthquake), the Wenchuan Earthquake Fault Scientific Drilling project in China (the 2008 Mw 7.9 Wenchuan earthquake), and the Japan Trench Fast Drilling Project in Japan (the 2011 Mw 9.0 Tohoku earthquake) were conducted ~ 1 –5 years after the earthquakes occurred (Ando, 2001; Fulton et al., 2013; Li et al., 2015; Ma et al., 2006). In addition, the San Andreas Fault observatory at depth in the USA, the Deep Fault Drilling Project for the Alpine Fault in New Zealand, and the Nakai Trough Seismogenic Zone Experiment in Japan were carried out during their interseismic periods (Sutherland et al., 2017; Tobin et al., 2019; Zoback et al., 2011). Fault drilling campaigns are a unique way to access seismogenic faults under in situ pressure and temperature conditions; therefore, these campaigns provide fresh fault materials and important data for understanding the geological structure and physical properties within and around fault zones, deformation mechanisms, role of fluids in fault lubrication, and stress conditions in seismogenic zones (e.g., Ikeda, 2001; Li et al., 2013, 2014, 2016; Lin et al., 2013; Nishiwaki & Lin, 2019; Townend et al., 2013; Yeh et al., 2007; Zoback et al., 2007).

The FFDP with one mostly vertical borehole and two inclined penetrating boreholes was conducted in 2017–2018 by Kyoto University (2018) mainly to obtain fresh fault rock samples from the Futagawa fault zone, newly

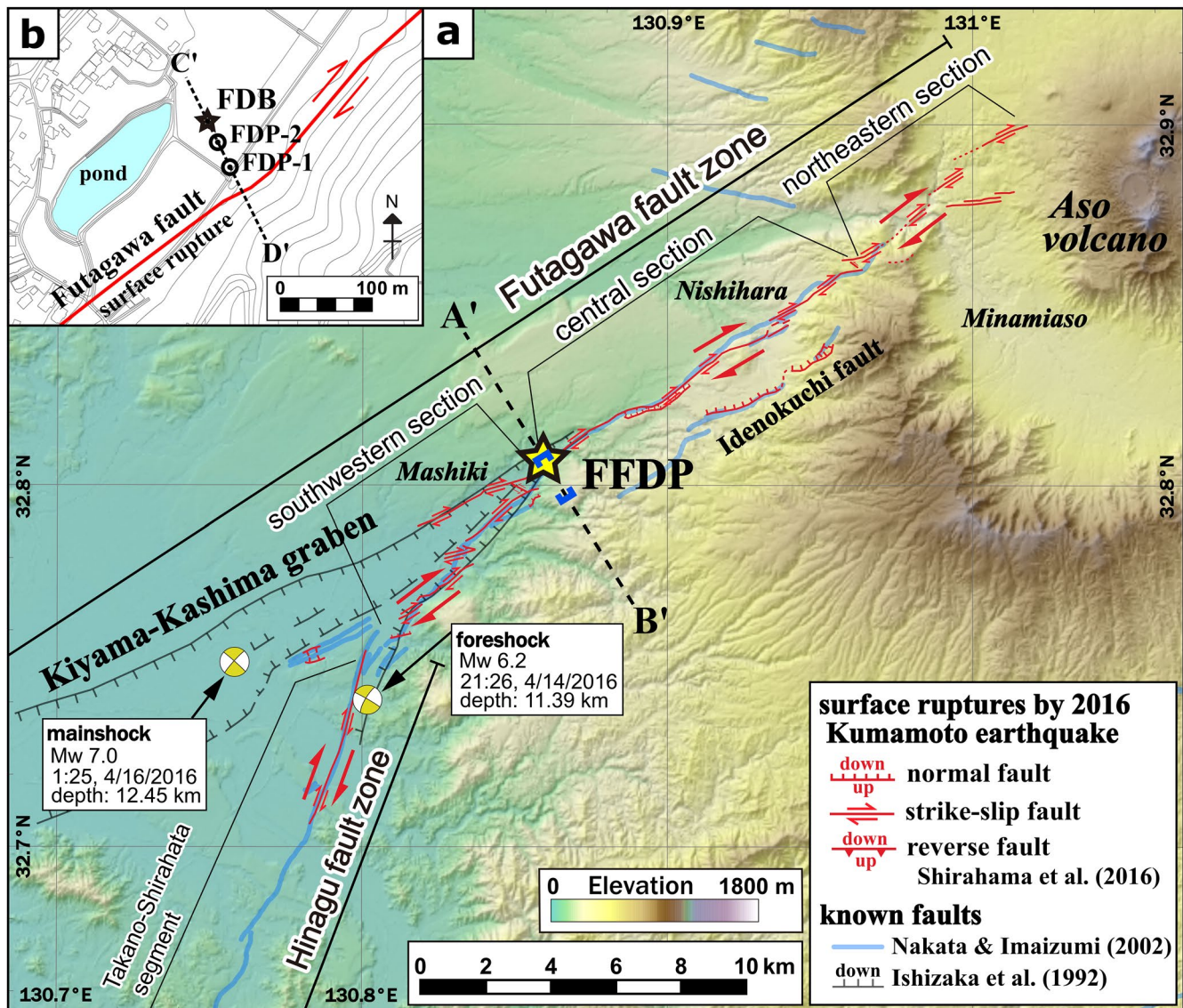


Figure 2. Topographic map of the Futagawa fault and the Futagawa fault drilling project (FFDP) site. Panel (a) was modified from Shirahama et al. (2016); and panel (b) was created based on 5-m-mesh digital elevation model data and basic items from the Geospatial Information Authority of Japan (2017). (a) FFDP site including FDB, FDP-1, and FDP-2 boreholes (yellow star after Kyoto University, 2018), surface ruptures associated with the 2016 Kumamoto earthquake sequence (red lines after Shirahama et al., 2016), known active faults before the 2016 Kumamoto earthquake (blue lines after Nakata & Imaizumi, 2002), and Kiyama-Kashima graben (black lines after Ishizaka et al., 1992), and the epicenters of the mainshock and the foreshock (yellow beach balls). The times of the earthquake occurrences are in Japan time. A'–B' broken line shows location of the geological cross-sectional profile (Figure 3). A pair of blue brackets to indicate the range of 1.5 km on the line of A'–B' shows range of occurred relative vertical displacement of ~1.4 m calculated by Moya et al. (2017). (b) Detailed locations of the boreholes FDB, FDP-1, and FDP-2. C'–D' broken line show location of the FFDP site geological cross-sectional profile (Figure 4). Red line is the surface rupture of the mainshock.

ruptured during the 2016 Kumamoto earthquake mainshock. Drilling occurred at the FFDP site in the town of Mashiki, where the surface rupture attained a maximum dextral slip (~2.2 m; Figure 2b). Here, we present the results of geological analysis of data collected from multiple boreholes penetrating the Futagawa fault zone. Our analysis, based on both core and logging data, provides insights into the key geological structures and physical property distribution of the active Futagawa fault zone at depths of several hundred meters. The results suggest a drastic change in the faulting pattern of the Futagawa fault before and after ~87 ka, probably related to the change in volcanism of Aso Volcano in the subduction system between the Philippine Sea and Eurasian plates.

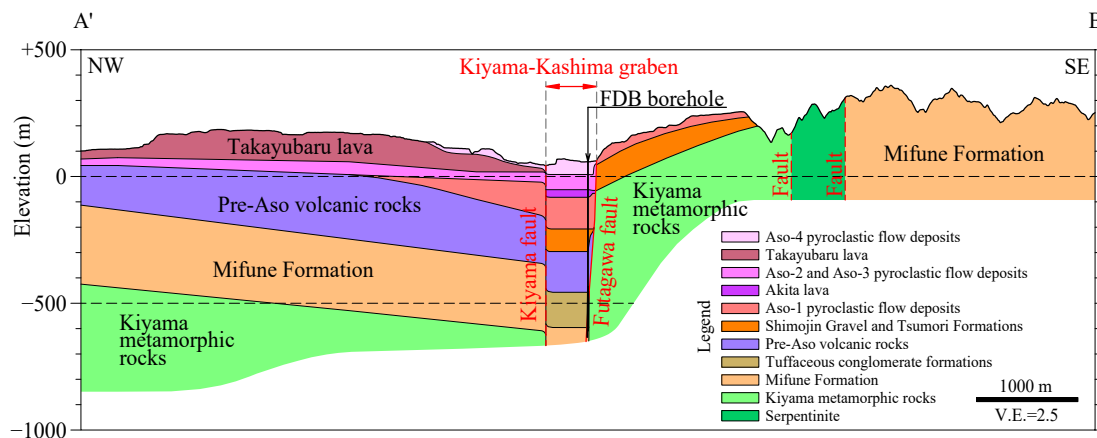


Figure 3. Geological cross-sectional profile of ~10 km-wide through FDB borehole. Refer to Figure 2a for the locations of A' and B'. Lithology and faults were constructed based on FDB cores of Kyoto University (2018) and wide geological cross sections of Nakayama et al. (2019). Surface geological distribution was based on a geological map of Hoshizumi et al. (2004); and the topographic line was created based on 5-m-mesh digital elevation model data from the Geospatial Information Authority of Japan (2020). V.E. denotes vertical exaggeration.

2. Geological Setting

The Futagawa fault is part of the Futagawa-Hinagu fault zone and is located within the active Aso volcanic region. The Futagawa fault is an active fault that triggered the mainshock of the 2016 Kumamoto earthquake sequence, which extended from the hypocenter for ~28 km to the western edge of the Aso caldera (Shirahama et al., 2016; Figure 2a). An ~450 m-wide depression that runs along the Futagawa fault in this study area is known as the Kiyama-Kashima graben (e.g., Ishizaka et al., 1992; Watanabe et al., 1979), and the FFDP site is located on the southeastern margin of this graben. The northwestern margin of this graben is located on a presumed fault called the Kiyama fault (e.g., Ishizaka et al., 1992). To better understand the structural geology surrounding the Futagawa fault, we created an ~10 km-wide geological cross-sectional profile in a north-west-southeast direction approximately orthogonal to the 2016 surface rupture around the FFDP site; this profile crosses the graben and faults (Figure 3). We mainly used information based on core descriptions from the FFDP described later and referred to a published geological map set including a 36 km-wide cross-sectional profile in the east-west direction and a 48 km-wide cross-sectional profile in the north-south direction, as well as a surface geological map (Hoshizumi et al., 2004; Kyoto University, 2018; Nakayama et al., 2019). As shown in Figure 3, the graben between the Kiyama fault and Futagawa fault results from a down-dropped block between the two faults via large vertical displacement, attaining a few hundred meters of subsidence relative to the footwall blocks either side of the graben.

Pyroclastic flow deposits erupting from Aso Volcano are widely distributed across the surface outside of the Aso caldera, including the FFDP site (e.g., Takarada & Hoshizumi, 2020). The FFDP site is located west-southwest of Aso Volcano ~10 km away from the edge of the caldera (Figure 2a). Aso Volcano is one of the most active volcanoes on the Japanese islands and had four large pyroclastic eruptions during the caldera-forming stage. The K-Ar ages of the four pyroclastic eruptions are 89 ± 7 ka for Aso-4, 123 ± 6 ka for Aso-3, 141 ± 5 ka for Aso-2, and 266 ± 14 ka for Aso-1, as determined by Matsumoto et al. (1991) and Matsumoto (1996), and are in close agreement with the defined ages based on tephra analysis by Aoki (2008) and Albert et al. (2019). The age of the Aso-4 eruption was determined to have a tephra age of 86.8–87.3 ka by oxygen isotope chronology (Aoki, 2008) and 86.4 ± 1.1 ka by $^{40}\text{Ar}/^{39}\text{Ar}$ dating (Albert et al., 2019), and an average of 87 ka was given by Tsuji et al. (2018). Therefore, we adopt this average age of ~87 ka as a representative value of the Aso-4 eruption. The Aso-4 pyroclastic eruption was the second largest in the world (Takarada & Hoshizumi, 2020); after this M8 supereruption the central volcanic cone group in the Aso caldera continued minor activities. The surface lithologies around the FFDP site include Aso pyroclastic flow deposits (Aso-4 and/or Aso-3), Takayubaru lava flows and old river sediments (fluvial deposits) on the northwestern side (hanging wall) of the Futagawa fault. The surface lithologies on the southeastern side (footwall) of the fault include Aso pyroclastic flow deposits (Aso-1), Quaternary sedimentary rocks (Shimojin Gravel and Tsumori Formations), upper Neogene to lower Quaternary Pre-Aso volcanic rocks, upper Cretaceous sedimentary rocks (Mifune Formation), and Paleozoic metamorphic

Table 1
Borehole Locations at Ground Surface, Depths, and Others for FDP-1, FDP-2, and FDB

Borehole name	Latitude	Longitude	Elevation of wellsite (m)	Distance from wellsite to SR ^a (m)	Borehole deviation angle (°)	Deviation azimuth (°)	True vertical depth (MD ^b)
FDP-1	32°48'20.8"	130°51'37.3"	59.3	30	20	160	~112.8 (~120.0)
FDP-2	32°48'21.7"	130°51'36.8"	58.0	60	12	160	~195.6 (~200.0)
FDB-1					0.8	90	~666.1 (~666.2)
FDB	32°48'22.3"	130°51'36.4"	58.0	81			454.0–691.6 ^c
FDB-1R					1.2	350	(454.0–691.7)

Note. FDP-1 and FDP-2 are deviated boreholes; but FDB-1 is a vertical borehole and FDB-1R is a sidetrack of FDB-1.

^aSR denotes the surface rupture formed during the 2016 Kumamoto earthquake mainshock. ^bMD is the measured depth. ^cThe depth range shows the drilled depth range of the branch borehole FDB-1R (Figure 5).

rocks (Kiyama metamorphic rocks; e.g., Hoshizumi et al., 2004). The Aso pyroclastic flow deposits on the hanging wall side of the Futagawa fault are younger than those on the footwall side.

The geological distributions differ greatly between the northwestern and southeastern sides of the Kiyama-Kashima graben (Figure 3). On the southeastern side of the Futagawa fault, the Shimojin Gravel Formation, Tsumori Formation, and basement Kiyama metamorphic rocks are found below the Aso pyroclastic flow deposits. On the northwestern side of the Kiyama fault, the Pre-Aso volcanic rock body and Mifune Formation are thickly distributed below the Aso pyroclastic flow deposits. Geological formations similar to those found northwest and southeast of the Kiyama-Kashima graben are all present in the graben.

Along the 2016 mainshock surface rupture, trench excavations at ≥ 10 sites in and out of the Aso caldera, including one site near the FFDP site, were conducted after the 2016 Kumamoto earthquake sequence (e.g., Toda et al., 2019). These results suggested a dominantly dextral strike-slip faulting mode for the 2016 mainshock event. Similarly, fresh horizontal slickenlines with 3–16° plunges suggesting strike-slips were observed in an outcrop ~500 m from the FFDP site soon after the earthquake (Oohashi & Tamura, 2016). In addition, one to four paleoseismic events prior to the 2016 earthquake in the past ~10,000 years were detected on the Futagawa fault from trench excavation observations and radiocarbon dating results, and a recurrence interval of ~2,000–4,000 years was inferred. On the other hand, Yano and Matsubara (2017) determined a dip of ~75°NW for the Futagawa fault based on the locations of seismicity that occurred from 14 April to 31 August 2016. This steep dip also corresponds to the fault dip through the finite difference method using radon-222 (Rn) concentration data in soil gas obtained on survey lines mostly orthogonal to the fault strike (Koike et al., 2009). The spatial distribution of Rn concentrations in soil gas is changeable with fault dip, because the gas carrying Rn ascends mainly through permeable fault zone. Fault dip was determined so that the calculated Rn concentrations near the surface were almost equal to the distribution of measured concentration data. Thus, the Futagawa fault was identified as a northwest steeply dipping fault by different research methods.

3. Drilling and Logging Overview

3.1. Drilling

In the FFDP from 2017 to 2018, two pilot boreholes, namely, FDP-1 and FDP-2, and the main borehole FDB, including FDB-1 and its branch FDB-1R, penetrated the Futagawa fault (Kyoto University, 2018). The borehole locations (latitudes, longitudes, and elevation of well sites and distances to the fault surface rupture), depths, and other parameters for all boreholes are summarized in Table 1 and illustrated in Figures 2b and 4. The three borehole locations were arranged in a northwestward direction approximately orthogonal to the surface rupture, that is, in the dip direction of the Futagawa fault plane (Figure 2b). The Futagawa fault at these locations is considered to be deeply fractured and acts as an ascent pathway for crustal gas based on the findings of anomalous concentrations of helium in the groundwater (Sano et al., 2016) and radon in the soil gas (Koike et al., 2014). In the first phase of this drilling project, the depths of the faults in FDP-1 and FDP-2, the dip of the fault plane, and the shallow geological structure were confirmed by the two fully cored pilot boreholes. FDP-1 and FDP-2 were drilled to total measured depths of 120 m and 200 m, respectively, and penetrated the fault plane at measured depths of

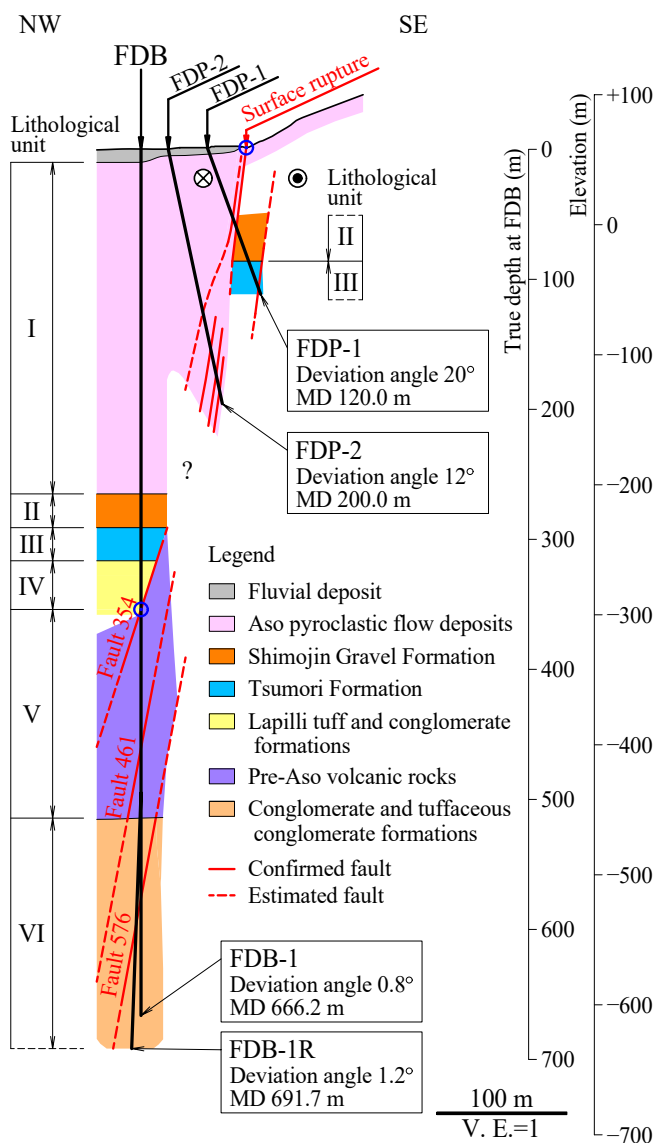


Figure 4. Geological cross-sectional profile around the Futagawa fault drilling project site. Lithology and faults of the cross section were constructed based on the cores obtained from FDB-1, FDB-1R, FDP-1, FDP-2, and the cuttings from FDB-1 (Kyoto University, 2018). I–VI in left column show the lithological units; real and dashed red lines denote faults. The two blue circles on the surface rupture and the Fault 354 show two points of a straight line for estimation of the fault dip with normal faulting displacement. MD is the measured depth. The question mark “?” means that relations of the faults observed in different boreholes were not confirmed. V.E. denotes vertical exaggeration.

65.6 and 177.4 m, respectively; the fault plane was inferred to connect to the surface rupture of the 2016 Kumamoto earthquake (Kyoto University, 2018).

In the second phase, the vertical main borehole FDB was drilled ~81 m northwest of the surface rupture (Figures 2b and 4). The main borehole drilling operation consisted of two stages. In the first stage, after drilling from the surface to 302 m without coring but with collecting cuttings for each 10 m and installing a casing, full coring was performed through the Futagawa fault to a total depth of 666 m (Figure 5). Then, downhole physical logging was conducted in the open hole depth interval from 302 to 662 m. This drilling borehole is referred to as FDB-1. FDB-1 is a mostly vertical well, and its deviation angle and azimuth are 0.8° and N90°E, respectively. In the second stage, following cementing to fill the open hole interval from the bottom to a depth of ~302 m, sidetrack drilling, termed FDB-1R, was carried out to obtain more core samples. FDB-1R gradually deviated from 454 to 495 m, then drilled down to a total depth of ~692 m and cored natural rock samples (Figure 5). We call both FDB-1 and FDB-1R the main borehole FDB.

Combining the FDB-1 and FDB-1R boreholes, continuous coring was conducted in depth intervals from 302 to 692 m with a core recovery rate of 96.5%. Core drilling from 302 m for borehole FDB-1 started on 24 January 2018, and was completed for FDB-1R at 692 m on 23 March 2018. Wireline coring was conducted using an HQ-type core bit with an outer diameter of 98.4 mm and an inner diameter of 63.5 mm for both FDB-1 and FDB-1R. During the first drilling stage, drilling mud was normally circulated within a depth interval of ~302–357 m, but mud loss occurred frequently at depths of ~357–380 m. Therefore, cementing was carried out to prevent mud loss when the bottom depth reached ~380 m. However, this countermeasure failed, probably due to an unstable borehole wall situation; thus, almost all injected drilling mud was lost below a depth of ~380 m.

To examine slip displacement on the Futagawa fault, we observe all the core samples in the drilling project. In addition, to reveal the characteristics of fault damage, we newly counted natural fractures and calculated fracture density for depths from ~302 to ~666 m in FDB-1. Secondary fractures created by drilling in the core samples were excluded from our fracture counting.

3.2. Logging

A campaign of wireline downhole geophysical logging in the FDB-1 borehole was performed twice for different depth intervals when the open borehole was filled by drilling mud (mud-added materials; polymer mud and bentonite, resistivity of drilling mud = 52.1 Ω-m, mud density = 1,010 kg/m³). The first log operation was conducted within a shallow depth interval from 302 to 383 m, but the log tools failed to reach below 383 m due to borehole wall collapse. In the second operation, the logs were successfully conducted in a depth interval ranging from 399 to 662 m after a drill rod was tentatively inserted down to the collapsed interval of the borehole wall. Therefore, log data, excluding the temperature, were not available within a depth interval of

383–399 m. For each depth interval, five runs, including (a) a temperature log, (b) an electrical log consisting of resistivity and spontaneous potential, (c) a caliper log, (d) a borehole televiewer (BHTV) log, and (e) sonic and natural gamma ray logs, were conducted successively by Geophysical Surveying Co., Ltd. (<https://www.gsct.co.jp/>). The digital log data were sampled at an interval of 10 cm.

The four-arm caliper log provided continuous measurements of two borehole diameters in orthogonal directions. The temperature log measured borehole temperatures using a thermistor sensor (0.1°C resolution) by lowering

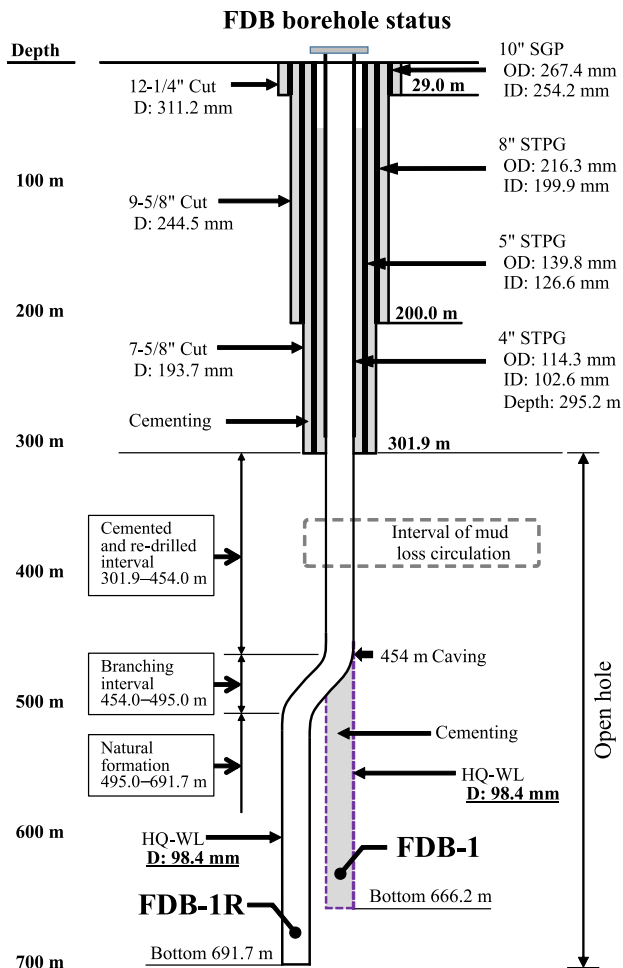


Figure 5. Final construction diagram for borehole FDB-1 and FDB-1R (based on the drilling records from Kyoto University [2018]). The abbreviations in the figure are shown below: SGP, steel gas pipe; STPG, steel tube pipe general; D, diameter; OD, outer diameter; ID, inner diameter.

the log tools at a constant rate of ~ 10 m/min. The temperature log of the second operation was conducted ~ 24 hr after the drilling operation when almost all circulation had been lost. The temperature of the mud in the wellsite mud tank, that is, before injection into the borehole, was 15.8°C . The spontaneous potential (SP) log measured the difference in electrical potential between an electrode moving along the borehole and a reference electrode fixed on the ground surface and was conducted with resistivity logging. The SP value arises mainly from electrochemical effects when fluids of different salinities are mixed, such as drilling mud and pore water in rocks. Natural gamma ray logs recorded natural radioactivity, but the tool used in the FFDP could not distinguish the contributions from uranium, thorium, and potassium individually and simply outputted a total count rate.

The resistivity log measured the electrical potential by passing a constant electric current through the borehole wall and calculating the resistivity of the rocks around the borehole. The normal resistivity log applied was measured at two electrode intervals of 25 cm (short normal; SN) and 100 cm (long normal; LN). The sonic log measured the travel time of the P-wave (primary wave) propagating in the rocks around the borehole. The measurement probe consisted of an ultrasonic transmitter and four receivers attached at distances of 60, 80, 100, and 120 cm from the transmitter.

The BHTV log measured two types of reflected sonic wave parameters, that is, intensity (amplitude value) and arrival time (travel time), from the borehole wall (Figure 6). The amplitude value is low for fractures and/or softer wall rocks and high for harder rocks without fractures. The amplitude values and travel times are expressed on a color scale, and the borehole wall can then be continuously imaged. Strikes and dips of fractures that appear on the unrolled images as sine curves can be read from the BHTV images (see Figure 6). We extracted natural fractures from the BHTV images in the logged depth intervals of FDB-1. Fracture analysis can accurately extract fractures in hard rocks such as andesitic lava. However, soft sedimentary rocks have smaller reflecting amplitudes and a lower contrast, thus making the extraction of fractures more difficult than in hard rock formations.

4. Lithology and Stratigraphy

Six main lithological units were defined using core samples from boreholes FDP-1, FDP-2, FDB-1, and FDB-1R (see the lithological units shown in Figure 4 and representative examples of core pictures for all the units and subunits shown in Figure 7). The lithologies at true depths from 0 m to 692 m were determined based on core samples from FDP-1, FDP-2, FDB-1, and FDB-1R, combined with analysis of cuttings from FDB-1. The lithological units between a true depth range from 196 m (the bottom of FDP-2) to 302 m (the top of the coring interval at FDB-1) were identified based only on cutting samples from FDB-1. The lithologies at the FFDP site consist of the Aso pyroclastic flow deposit (Unit I), Shimojin Gravel Formation (Unit II), Tsumori Formation (siltstone and sandstone, Unit III), lapilli tuff and conglomerate formation (Unit IV), Pre-Aso volcanic rock body (Unit V), and a conglomerate and tuffaceous conglomerate formation (Unit VI) considered to be Lahar deposits. The fault plane that ruptured during the 2016 Kumamoto earthquake mainshock was preliminarily considered to be located within the depth interval from 354 to 576 m (Kyoto University, 2018). Abundant brown clays with slickenlines filling in fracture-like structures were observed in a depth interval ranging from 457 to 510 m (see an example of subunit Vc shown in Figure 7). Referring to each lithological unit, units I to III were confirmed in FDP-1, unit I in FDP-2, units III to VI by core samples in FDB-1, and units V to VI in FDB-1R. The characteristics of the six main lithological units based on drill core descriptions are described below.

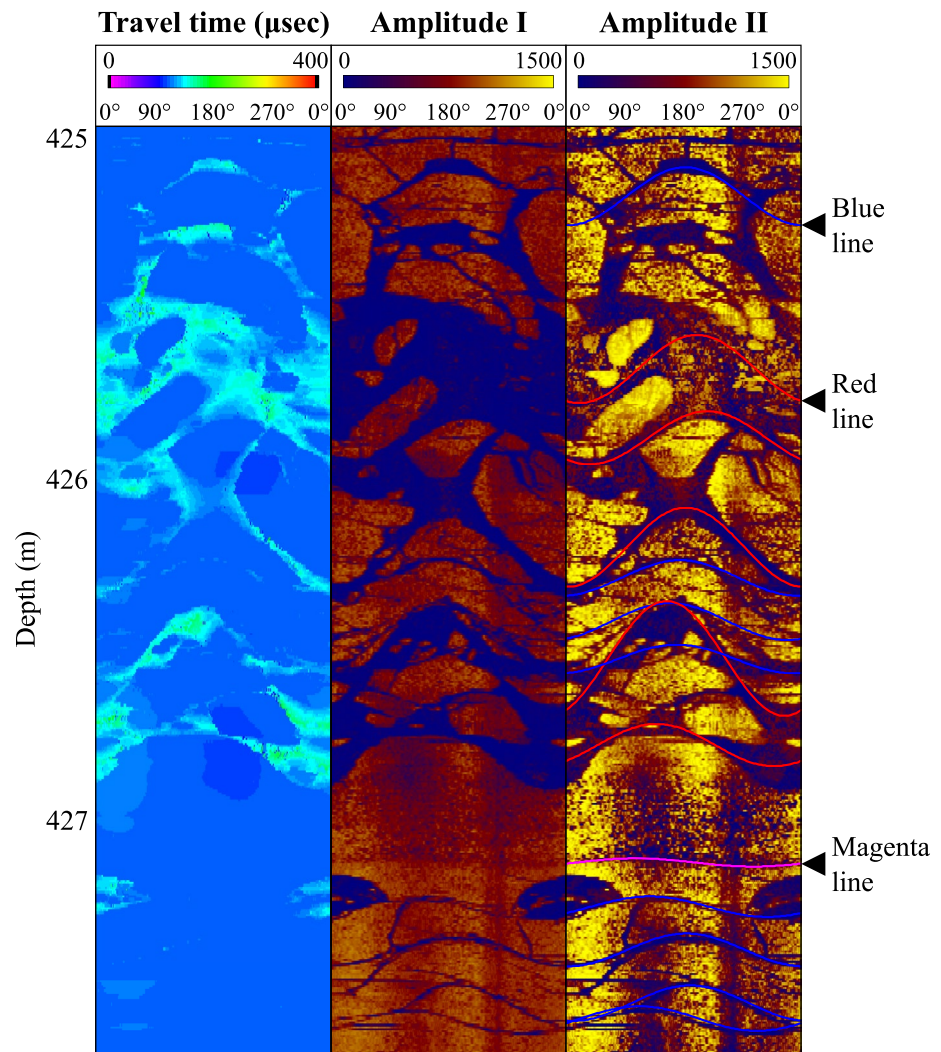


















Figure 6. A borehole televiewer images of the FDB-1 borehole (modified from Kyoto University [2018]). Amplitude I and II denote static and dynamic images, respectively. The sine curves on Amplitude II panel are the records of fracture picking to count fracture numbers and to determine fracture's dip azimuth and angle of dip. Colors of the sine curves denote categories of the fracture certainty; red lines show clear fractures, blue lines are slightly unclear fractures, and magenta lines are lava flow structures.

4.1. Unit I (Aso Pyroclastic Flow Deposits)

The Aso pyroclastic flow deposits are products of major Pleistocene volcanic eruptions from Aso Volcano (e.g., Takarada & Hoshizumi, 2020). The deposits with a large thickness of ~255 m at the FFDP site were divided into four eruptive units, that is, Aso-4, Aso-3, Aso-2, and Aso-1, in order of increasing age, which is the same as the order of increasing depth (Figures 8a and 8b). In addition, a thin lava bed referred to as the Akita (Ak) lava (~12–30 m in thickness determined from FDP-2 cores and FDB-1 cuttings) is present between Aso-2 and Aso-1.

The Aso-4 pyroclastic flow deposit is pumiceous and exhibits grayish white to pale yellowish brown colors. This deposit includes a large amount of white, porous pumice in fine-to medium-grained ash. The rock fragments consist of andesite and mudstone. In the lowest part of the pyroclastic flow deposit, conglomerate and pumiceous tuff were observed in FDP-2 but were absent in FDP-1. The Aso-3 pyroclastic flow deposit is scoriaceous nonwelded tuff and weakly welded tuff. This deposit is composed of black to pale red fine-to medium-grained ash, various rock fragments, scoria, and pumice. The Aso-2 pyroclastic flow deposit is scoriaceous welded tuff. The deposit is

Unit/Subunit		Core photo	Borehole ID, Core top depth, Rock type
I	Aso-4		FDP-2, 40.1 m, Pumiceous pyroclastic flow deposit
	Aso-3		FDP-2, 68.2 m, Scoriaceous pyroclastic flow deposit
	Aso-2		FDP-2, 106.2 m, Welded pyroclastic flow deposit
	Ak		FDP-2, 123.3 m, Andesitic lava
	Aso-1		FDP-2, 162.1 m, Strongly welded pyroclastic flow deposit
II	-		FDP-1, 83.5 m, Gravel (semiconsolidated conglomerate)
II/III	-		FDP-1, 92.5 m, Unit boundary of II and III (Red arrows)
III	-		FDB-1, 314.6 m, Siltstone and sandstone
IV	IVa		FDB-1, 326.0 m, Lapilli tuff
	IVb		FDB-1, 332.5 m, Conglomerate
V	Va		FDB-1, 373.4 m, Autobrecciated andesitic lava
	Vb		FDB-1, 439.1 m, Andesitic lava
	Vc		FDB-1, 500.5 m, Autobrecciated andesitic lava
VI	VIa		FDB-1, 541.4 m, Conglomerate
	VIb		FDB-1, 638.4 m, Tuffaceous conglomerate
			FDB-1, 663.0 m, Greenschist-rich breccia

Length of each core is 50 cm for FDP-1 and FDP-2, and 40 cm for FDB-1.

Figure 7. Core photos of typical rocks in the Futagawa fault drilling project site from the FDB-1, FDP-1, and FDP-2 boreholes (Kyoto University, 2018). The numbers of depths are the measured depth in the individual boreholes. The red arrows show the boundary between units II (Shimojin Gravel Formation) and III (Tsumori Formation).

composed of essential scoria and a scoriaceous ash matrix characterized by black fine-to medium-grained volcanic crystalline grains and fewer rock fragments. The Aso-1 pyroclastic flow deposit is mostly strongly welded tuff. The welded tuff is composed of glassy fine-to medium-grained ash and abundant lithic fragments and is highly consolidated; it appears grayish white to black.

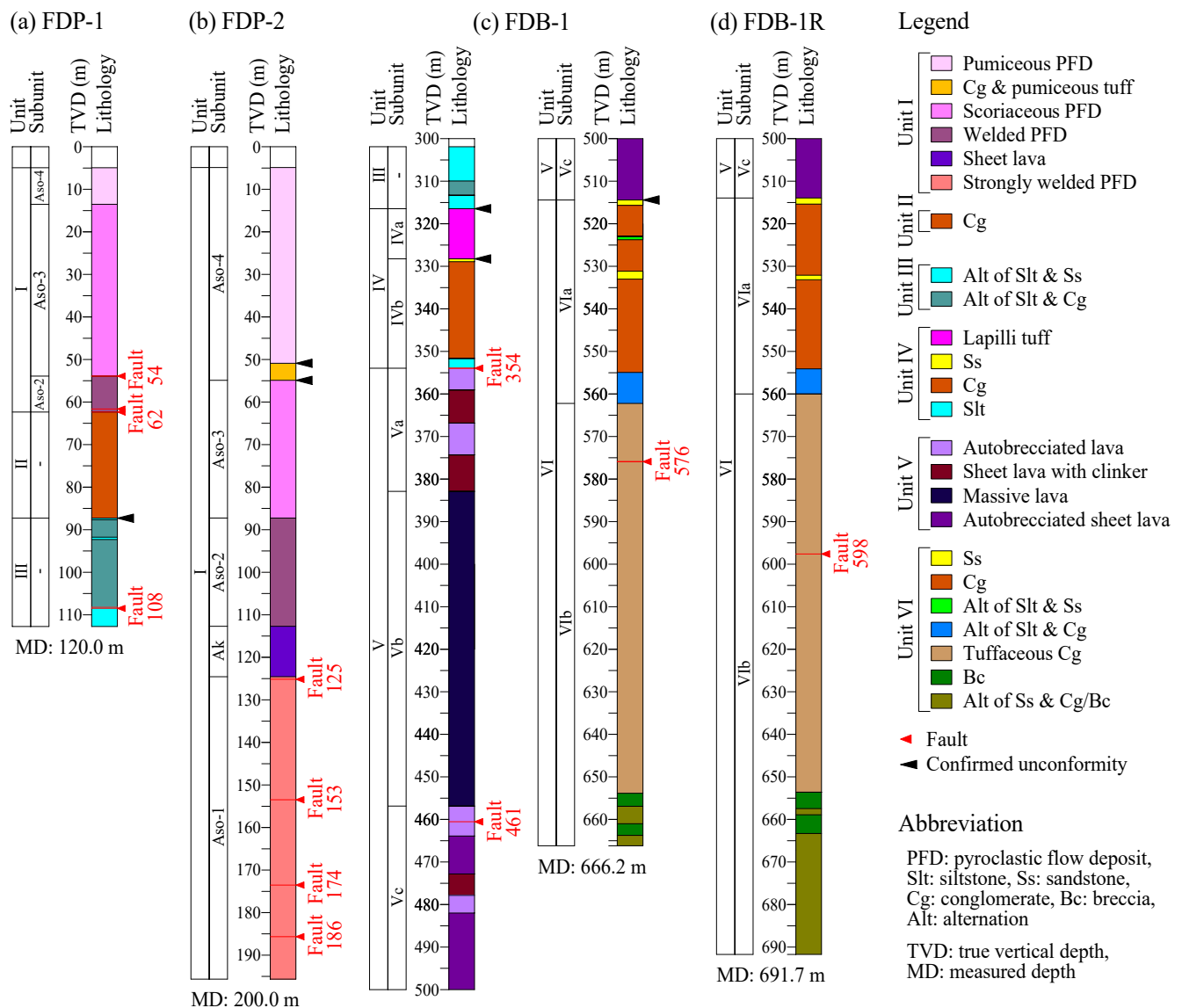


Figure 8. Lithological columns of FDP-1, FDP-2, FDB-1, and FDB-1R based on core descriptions in a true vertical depth scale. “Fault” and number denote depths of main slip planes.

4.2. Unit II (Shimojin Gravel Formation)

The Shimojin Gravel Formation was observed in depth intervals of ~66–93 m (corresponding to true depths of ~62–87 m) and ~265–291 m in FDP-1 and FDB-1, respectively, and is a characteristic gravel layer consisting of circular to subcircular pebbles and cobbles originating from volcanic rocks distributed around the study site. It is known to be distributed below the Aso pyroclastic flow deposits (Unit I) and above the Tsumori Formation (Unit III; e.g., Imanishi, 1967; Watanabe & Ono, 1969). Therefore, the Shimojin Gravel Formation is considered a sedimentary formation in the middle Pleistocene (Hase & Iwauchi, 1993). A semiconsolidated matrix fills spaces between the gravel fragments and consists of clay and sand particles.

4.3. Unit III (Tsumori Formation)

The top and bottom of the Tsumori Formation were observed via core samples in FDP-1 and FDB-1, respectively. Its thickness at the FFDP site is estimated by cuttings and cores to be ~26 m. This formation is known to contain middle Pleistocene lake deposits (Hase & Iwauchi, 1992, 1993), including various index and facies

fossils, for example, freshwater diatoms (Tanaka et al., 2005) and insects (Hayashi et al., 2004). This formation observed in the FDB-1 core samples was characterized by brown to light brown alternations of siltstones and fine-grained sandstones and a few coarse-grained sandstone and conglomerate layers. The sedimentary layers observed in FDP-1 are mainly composed of alternations of laminated siltstones and conglomerates and siltstones and fine-grained sandstones. As a common facies in both boreholes, the siltstone contains parallel laminae, the depositional surfaces show almost horizontal or gentle inclinations of $<5^\circ$, and the sediments are not strongly consolidated. The characteristics of this facies are comparable to those described by Imanishi (1967), who first defined the Tsumori Formation. Overall, the facies as observed in the two boreholes is almost the same, although cores throughout the whole depth interval of the formation were not retrieved from FDP-1 and FDB-1.

4.4. Unit IV (Lapilli Tuff and Conglomerate Formations)

Unit IV was defined in a depth interval from 317 to 354 m in FDB-1 and subdivided into subunits IVa of lapilli tuff and IVb of conglomerate. Subunit IVa is a scoria-rich lapilli tuff formation. The lapilli tuff has characteristically black scoria with a maximum size of ~ 8 cm and is yellowish brown to grayish brown. The density of scoria gravels increases downward in the subunit. The facies is mostly massive with no bedding apparent. The gravel bed of subunit IVb is located below the lapilli tuff. The facies of subunit IVb contains many hard and fresh andesite boulders with a maximum size of ~ 50 cm and is similar to that observed in unit II. The boundary between the two subunits was characterized by an unconformity at ~ 328 m. A thin sand layer (~ 0.8 m in thickness) located immediately beneath subunit IVa has mostly coarse grains and is yellow-brown to brown and massive with no bedding apparent. The lower part of subunit IVb exhibits semiconsolidated pale-brown alternations of siltstone and fine sandstone (~ 2.3 m in thickness). Subunit IVb contacts the lower Pre-Aso volcanic rocks at a depth of 354 m.

4.5. Unit V (Pre-Aso Volcanic Rocks)

Unit V consists of volcanic rocks called the Pre-Aso volcanic rocks, which are older than the Aso pyroclastic flow deposits and were deposited before the Aso caldera-forming stage (e.g., Watanabe & Ono, 1969). The Pre-Aso volcanic rocks in this area consist of the products of andesitic volcanic activity, massive lavas, autobrecciated lavas, sheet lavas, and clinkers. The Pre-Aso volcanic rocks were deposited during the period from 6 to 0.35 Ma, but the volcanic activity producing the Pre-Aso volcanic rocks occurred mostly in the period from 0.8 to 0.35 Ma (e.g., Furukawa et al., 2009; Kaneoka & Suzuki, 1970).

Unit V consists of a hard massive andesitic lava layer and two altered andesitic lava layers with autobrecciated lavas and clinkers above and beneath the massive lava (Figure 8c). Therefore, this unit was subdivided into three subunits Va, Vb, and Vc by the differences in lithological characteristics. Subunit Va consists of altered andesite mainly composed of autobrecciated lavas and clinkers at depths from 354 to 383 m; subunit Vb is massive lava at depths from 383 to 457 m exhibiting gray to bluish-gray and red-purple colors in the weakly altered part; and subunit Vc is the autobrecciated altered lava within a depth range of 457–514 m. The autobrecciated lavas in subunits Va and Vc are extremely brittle and have yellow-white to reddish purple-white colors due to strong alteration. The clinkers generally alternate with lavas.

Unit V is a lithofacies with predominant fractures in FDB-1. Low-angle fractures are prominent at depths ranging from 389 m to 395 m, and numerous high-angle fractures were observed from 440 to 478 m. In subunit Vc, there are many fractures filled by semiconsolidated brown clay at depths of 460–472 and 495–503 m. The brown clay is homogeneous and has numerous strike-slip striations at the boundary with the host rock.

4.6. Unit VI (Conglomerate and Tuffaceous Conglomerate Formations)

Unit VI ranges from 514 m down to the bottoms of both FDB-1 (666 m) and FDB-1R (692 m) and was subdivided into subunits VIa and VIb (Figures 4, 8c, and 8d). The boundary between the two subunits was characterized by the presence of an ~ 7 m-thick alternation of siltstone and conglomerate, and is set at the bottom of the alternation (562 m in FDB-1). These lithofacies were confirmed at similar depths in both the FDB-1 and FDB-1R cores.

Subunit VIa is mostly semiconsolidated conglomerates located at depths ranging from 514 to 562 m. The uppermost part of the subunit consists of alternating fine sandstone and conglomerate with a thickness of 1.3 m, which was unconformably covered by Pre-Aso volcanic rocks (subunit Vc). The conglomerate contains numerous

rounded cobbles and boulders of andesite with sizes of 10–30 cm and angular greenschist pebbles and cobbles. The matrix of conglomerates is fine-to medium-grained gray to brown sandstone. The conglomerate layer is locally accompanied by a sandstone layer with a thickness of 1–2 m and shows low-angle bedding at 0–30°.

Subunit VIb is mostly consolidated tuffaceous conglomerate. The tuffaceous conglomerate does not have bedding structures and is grayish brown. Gravels in the conglomerate are composed of andesite subrounded-angular cobbles, boulders, and pebbles with sizes of ~10 cm or less, and the density of the black volcanic scoria fragments tends to increase downward in the subunit. The lowest part of subunit VIb deeper than 654 m in FDB-1 is accompanied by greenschist-rich breccia layers that are 3 m thick or less. The breccias are brittle and characterized by their composition of greenschist, serpentine, and quartz vein fragments. Greenschist-rich breccia alternates with green-gray-colored sandstone and conglomerate layers. In addition, this lithofacies was also confirmed deeper than 654 m in FDB-1R and tends to be accompanied by numerous conglomerate layers in the deep part (Figure 8d).

4.7. Faults

The candidate fault that ruptured during the 2016 Kumamoto earthquake mainshock is considered one of the three damage zones with sharp slip plane(s) intersected in FDB-1. The damage zones include the fault core, breccia, and fractured zone, and the depths of the damage zone centers (fault core or slip plane) are 354, 461, and 576 m, respectively (Figure 9). Here, we call the three damage/slip zones Fault 354, Fault 461, and Fault 576. Fault 354 is located at a lithological boundary between siltstone (subunit IVb) and autobrecciated lava (subunit Va) and is accompanied by a sharp slickenline slip plane (Figure 9a). We considered that the movement sense of the slickenlines resembled normal faulting because (a) the slip plane dips 80°WNW as derived by BHTV image and is almost parallel to the Futagawa fault estimated by surface rupture survey, seismicity, and coseismic surface displacement observations (Moya et al., 2017; Shirahama et al., 2016; Yano & Matsubara, 2017); (b) its slickenlines are mostly parallel with the dip direction of the slip plane (Figure 10a); and (c) the subsidence of the hanging wall of the Futagawa fault was confirmed (Figure 4). This normal faulting is not consistent with the dominant strike-slip faulting observed on the 2016 mainshock surface rupture at the FFDP site.

The damage zone at approximately 461 m (Fault 461) is considerably wider (~45 m in vertical thickness) than those of the other two damage zones (~3–6 m in vertical thickness), and three sharp slip planes were confirmed in the fault core depth interval from 460.4 to 460.6 m (Figure 9b). This damage zone is located in the uppermost part of subunit Vc (autobrecciated lava), only ~3.7 m below the boundary between subunits Vb and Vc. Within a slip plane dipping ~45° at a depth of ~460.3 m as an example, the presence of dominant strike-slip slickenlines (Figures 10b–10d), which have the same sense of movement as the surface rupture formed during the 2016 Kumamoto earthquake mainshock, was confirmed. In addition, semiconsolidated brown clays were observed within the fault core, breccias and fractured zone of Fault 461. Strike-slip slickenlines in approximately horizontal directions on steep slip surfaces as shown in Figure 10e, within semiconsolidated brown clays were confirmed at nine places or more in a depth range of 460.2–503.2 m.

Fault 576 is in the tuffaceous conglomerate (subunit VIb), and its fault core was confirmed within a depth interval ranging from 575.9 to 576.1 m (Figure 9c). A slip plane at a depth of 575.9 m in FDB-1 is oriented at a steep dip and has a yellowish-brown color along the slip plane. This slip plane does not cut straight through the drill core but is curved. An additional slip plane was observed at a depth of 576.8 m in this fractured zone, and the fracture density clearly decreases in the wallrocks below the slip plane. A damage zone similar to Fault 576 was confirmed at a depth of 597.6 m in FDB-1R, which is the branch borehole from FDB-1 (Figures 4 and 5).

5. Physical Properties From Geophysical Logging

Geophysical logging provides continuous records of lithological information and the in situ physical properties of the rocks surrounding the borehole (e.g., Doan et al., 2011; Goldberg, 1997). Composite depth profiles of seven parameters, a borehole wall image in the depth interval of ~302–662 m in FDB-1 and the fracture density derived from core descriptions and fracture attitude determined from BHTV images are illustrated in Figure 11. In particular, gamma ray index, the resistivity, and the P-wave velocity are known to correlate with lithofacies well. Natural gamma rays is used to discriminate lithofacies because of its dependence on the abundance of potassium. Resistivity and P-wave velocity are effective to discriminate damage zone because these reflect textural features

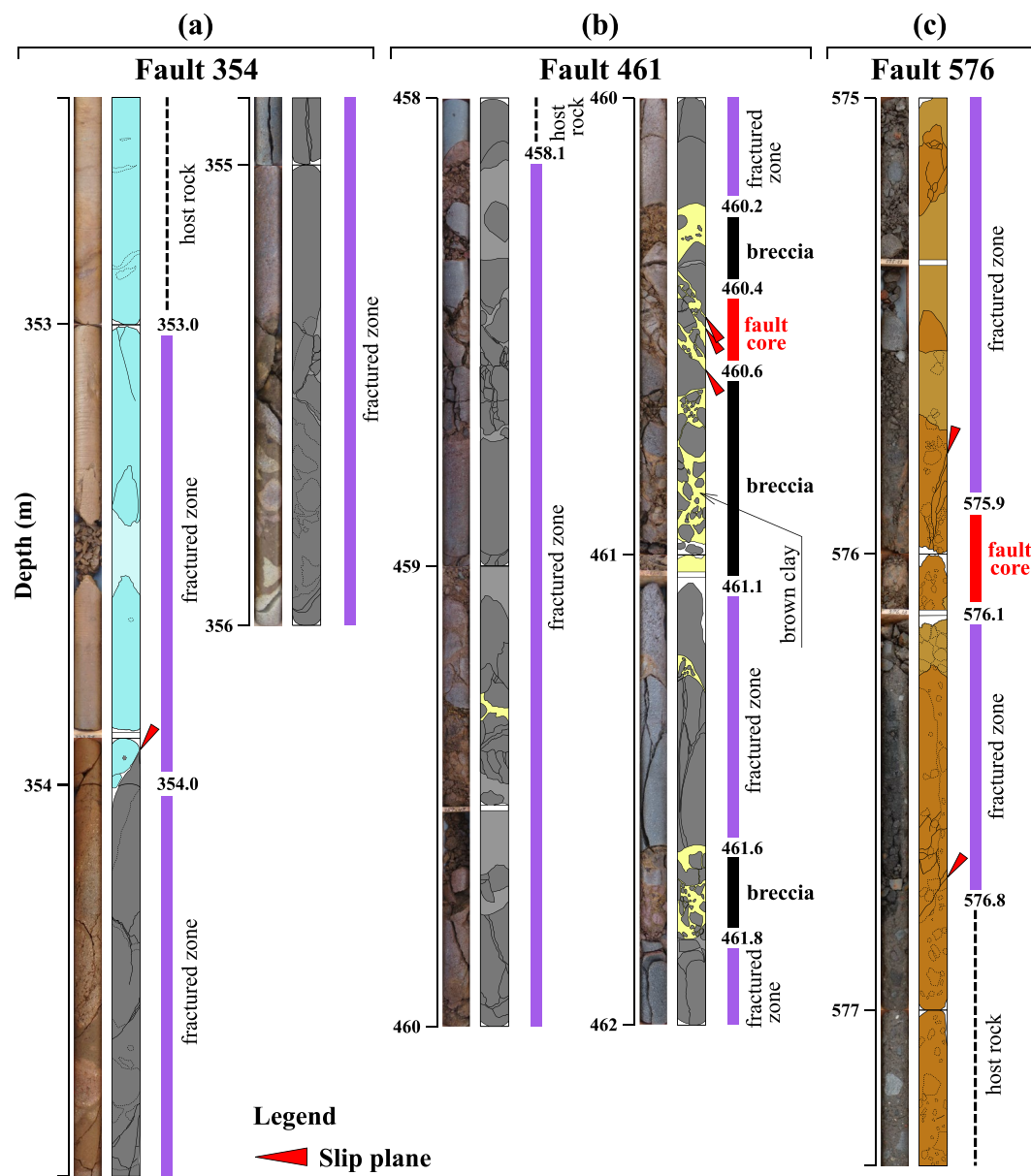


Figure 9. The core photos and sketches of the Fault 354, 461, and 576 penetrated in FDB-1, in depth ranges of (a) 352.5–356.0 m, (b) 458.0–462.0 m, and (c) 575.0–577.4 m, respectively. The core photos were originally obtained by the Futagawa fault drilling project (Kyoto University, 2018). The colors in the sketches for different rock types are: light blue for siltstone in unit IV, gray for autobrecciated lava in unit V, and brown for tuffaceous conglomerate in unit VI. Yellow color part shows brown clay filling gaps in breccia or fractured zone. The parts of cores with disturbance from drilling operations were shown by pale color in the sketches for the same color used for the same rock type of cores without disturbance.

(e.g., fracture networks) as well as lithofacies. In this study, the statistical values (mean and standard deviation) of these three representative physical properties to reveal the lithological characteristics in the physical properties of each subunit, in all the logged subunits are summarized (Table 2). As mentioned in the Section 3.2, log data excluding temperature are not available in the depth interval of ~383–399 m due to the failed installation of the log tools into this depth interval.

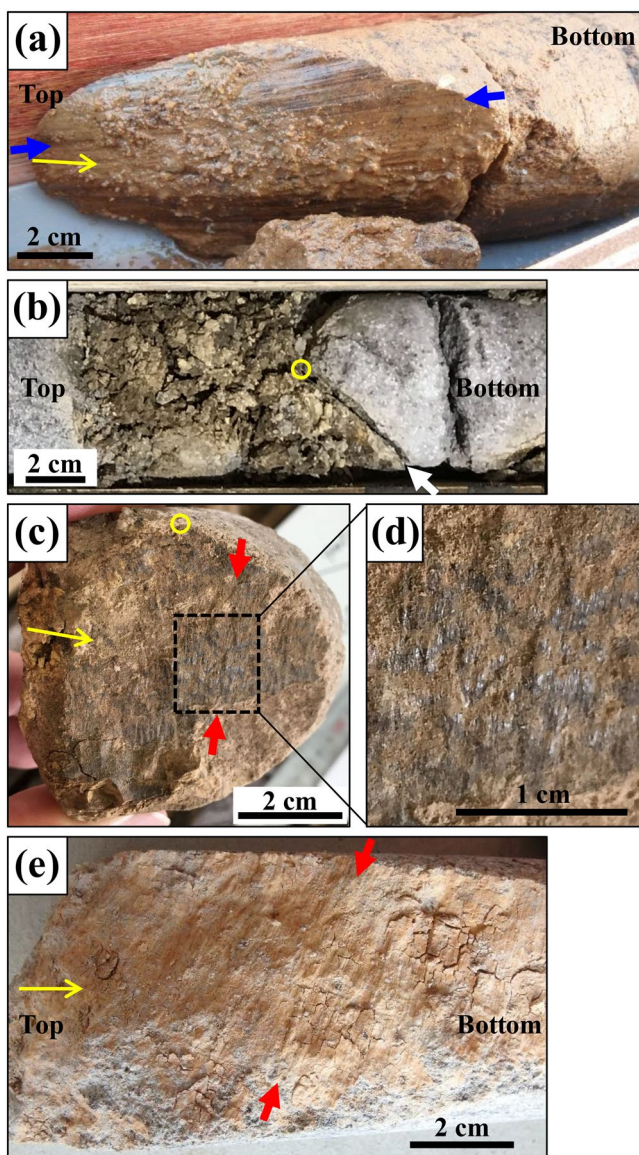


Figure 10. Core photos of slickenlines in the damage zones from the FDB-1 borehole (Kyoto University, 2018). The blue and red arrows show slickenlines. The yellow arrows show directions from the top to the bottom on the slip planes. The top/bottom mean to the upper/lower (shallower/deeper) sides of the core. (a) Dip-slip faulting slickenlines at a depth of ~354.0 m in the Fault 354. (b) Side view of the core shown in panels (c) and (d). The white arrow shows the slip plane dipping ~45° in panel (c). The yellow circle in this figure indicates the same position as the yellow circle in panel (c). (c) Strike-slip faulting slickenlines on a slip plane dipping ~45° at a depth of ~460.3 m in the Fault 461. (d) Enlarged view in area of broken-line rectangle in panel (c). (e) Strike-slip faulting slickenline structures in the clay-rich areas at a depth of 471.5 m.

(subunit VIa) and then remained almost constant (lower values of approximately 35 API) with a slight gradual increase down to the borehole bottom.

In comparison with natural gamma rays, the spontaneous potential was more variable and appeared to depend not only on the lithofacies but also on the textural features (e.g., fractures) of the rocks (Figure 11f). Specifically, it significantly and frequently changed in Unit V consisting andesite. In principle, the spontaneous potential is

5.1. Borehole Diameter and Temperature

The FDB-1 borehole in its coring and wireline logging depth interval from ~302 to 666 m was drilled using a 98.4 mm-outer diameter bit, and the borehole diameter should be ~100 mm if no collapse occurred. Results obtained by the four-arm caliper show that borehole diameters in two orthogonal directions expand to ~130 mm in parts of unit III and subunit IVa and to ~150 mm or more widely in subunits Va and locally in Vc. At depths where the borehole is expanded, almost equal diameters in two directions might suggest washouts instead of borehole breakouts. No caliper data are available in the depth interval of ~383–399 m, but the borehole wall in this depth interval might be more unstable than those in other intervals.

The temperature-depth profile obtained by the second log operation ~24 hr after the drilling of FDB-1 was completed under a state of circulation loss (assuming that ~16°C mud was cooler than the formation temperature) and revealed an anomalous feature that did not monotonically increase with depth, although the temperature might be influenced by the cooler circulation (Figure 11d). In general, the temperature deep underground, where it is not affected by weather, increases with depth due to heat flow from the deeper crust. The temperature, however, showed a near-constant value in the depth interval of ~330–390 m (approximately in subunits IVb and Va). As one possible reason, this phenomenon could have been caused by fluid flow in the borehole. In addition, the temperature at a depth of 435 m in subunit Vb revealed a negative peak, which was probably caused by the cooler mud flowing in this lost circulation zone. Below the subunit boundary between Vb and Vc (~457 m) in subunit Vc and Unit VI, the temperature gradient was nearly constant at ~40°C/km, which was slightly higher than the global average geothermal gradient of ~30°C/km (Sutherland et al., 2017). However, the temperature gradient distinctly increased in the deepest part of the borehole. To confirm the temperature distribution in the borehole, the temperature log should be repeated after the disturbed temperature recovers to the natural geothermal equilibrium state.

5.2. Natural Gamma Rays and Spontaneous Potential

Overall, natural gamma rays showed a strong correlation with lithofacies and varied within a range of ~25–60 API on average (Figure 11e and Table 2). The Tsumori Formation (Unit III) had a lower value of approximately 30 API, although siltstone generally has higher gamma radioactivity. In Unit IV, the natural gamma ray value gradually increased in lapilli tuff (subunit IVa) and then showed a higher value of 59 API on average in the conglomerate (IVb), but the siltstone layer near the unit boundary formed by Fault 354 indicated lower values of 25–50 API. In the andesite section (Unit V), the value did not change significantly compared to that in Unit IV but showed small changes in the autobrecciated lavas (subunits Va and Vc). Higher values in the massive lava interval (Vb) and a small stepwise change around the subunit boundary between Vb and Vc were revealed. Subunit Vb displayed the higher mean value of up to 59 API in all units/subunits of FDB-1 (Table 2). Natural gamma rays showed a significant decrease from andesite (unit V) to conglomerate

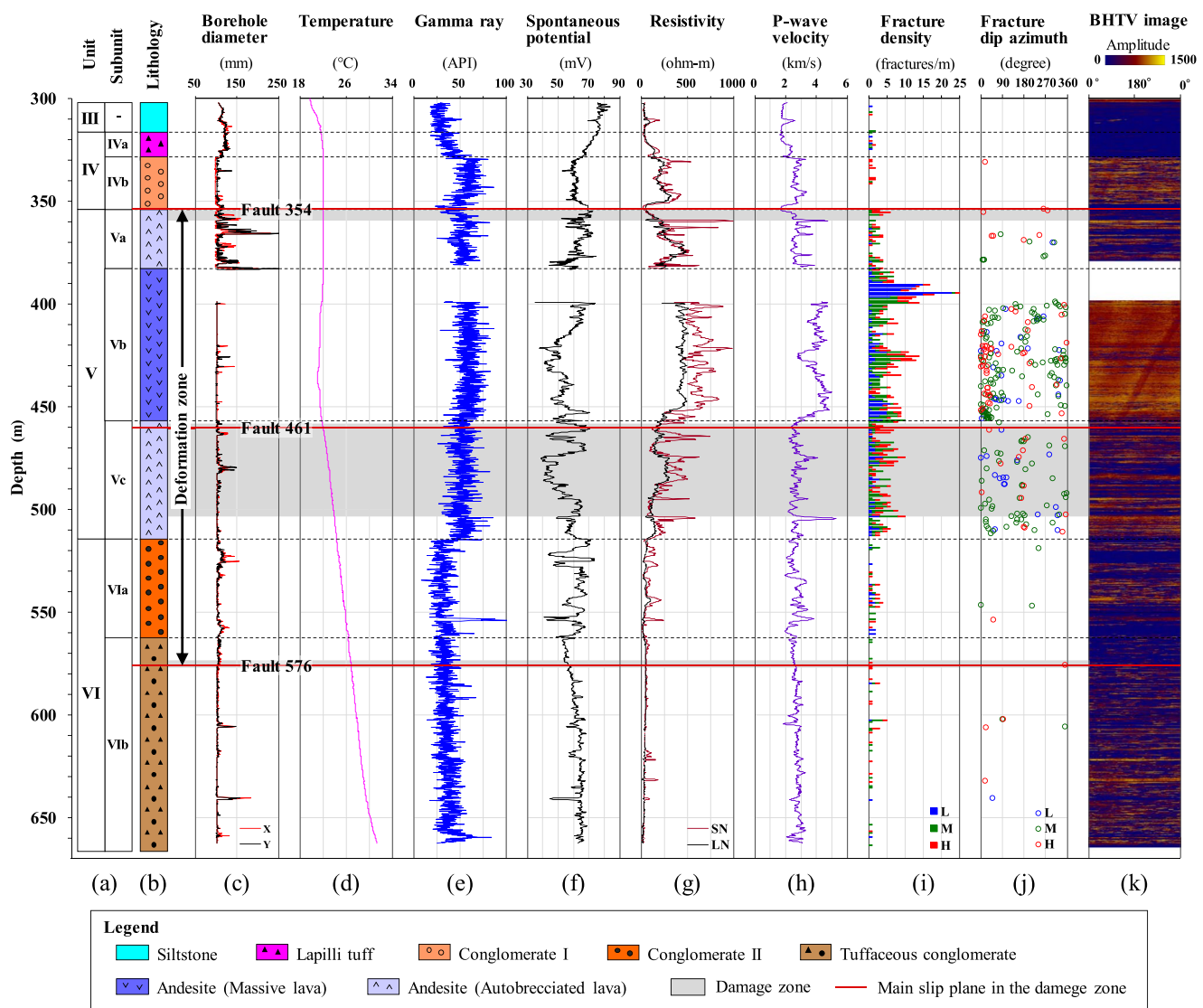


Figure 11. Composite depth profiles of physical properties and fracture parameters in the logged and cored depth ranges in FDB-1. (a) Lithological units and subunits, (b) lithological column, (c) borehole diameter, (d) temperature, (e) natural gamma ray, (f) spontaneous potential, (g) electrical resistivity, (h) P-wave velocity, (i) fracture density, (j) fracture dip azimuth, (k) and a BHTV amplitude image. SN and LN in panel (g) indicate short normal resistivity and long normal resistivity, respectively. L, M, and H in panel (i) and (j) indicate categories of fracture angles of dip; “L” means $<30^\circ$ from the horizontal plane; “M” for angles $\geq 30^\circ$ and $<60^\circ$; “H” for angles $\geq 60^\circ$. Data of Figures in panels (c–h, j, and k) were originally obtained by the Futagawa fault drilling project (Kyoto University, 2018).

generated by the salinity difference between drilling mud and formation porewater; therefore, it reflects the permeability of wallrocks and porewater resistivity. Overall, the changes in the spontaneous potential in the borehole revealed a reverse pattern but a high correlation with resistivity, especially with the SN resistivity, which is discussed below (see Figures 11f and 11g). The spontaneous potential showed higher values in Unit III consisting of siltstone but relatively lower values in andesite (Unit V). In addition, the spontaneous potential was relatively stable in the tuffaceous conglomerate (subunit VIb).

5.3. Resistivity

The resistivities of lithological units changed induced by both the lithofacies and textural features, especially those of connected pores (e.g., fracture networks) filled by pore water in the rocks. Generally, SN resistivity as the “shallow resistivity”, which is probably more dependent on the conditions present in the shallow part around the borehole, but LN resistivity measures the “deep resistivity,” reflecting the true resistivity of rocks beyond the

Table 2

Representative Physical Properties for All the Lithological Units and Subunits From Well Logging Below ~302 m in FDB-1 Borehole

Unit and subunit	Depth ^a (m)	Gamma ray (API)				Long normal resistivity (ohm-m)				P-wave velocity (km/s)				
		Range	Mean	SD	<i>N</i>	Range	Mean	SD	<i>N</i>	Range	Mean	SD	<i>N</i>	
III	–	301.9–316.5	18–40	27	5	75	27–48	34	4	66	1.7–1.9	1.8	0.0	75
IV	IVa	316.5–328.2	18–53	38	7	97	31–149	92	40	95	1.7–2.5	2.1	0.3	97
	IVb	328.2–354.0	32–87	59	9	215	146–328	226	42	215	2.3–3.4	2.7	0.2	215
V	Va	354.0–382.9	26–82	53	9	260	48–485	277	110	269	2.2–4.7	2.8	0.4	268
	Vb	382.9–456.9	29–87	59	9	562	221–514	433	56	562	2.8–5.0	4.0	0.5	562
	Vc	456.9–514.4	26–86	53	9	556	48–311	178	61	555	2.2–5.2	2.7	0.4	556
VI	VIa	514.4–562.2	8–56	31	7	362	22–105	50	17	332	2.0–3.5	2.7	0.3	362
	VIb	562.2–662.2	14–85	37	9	990	10–56	40	10	884	1.9–3.3	2.7	0.2	990

Note. Mean and SD (standard deviation) were calculated for number of data (*N*) excluding values near lithological boundaries and several short depth intervals where the lithologies differs with that of the unit/subunit; for an example, data of a ~2 m thickness siltstone layer in the subunit IVb (conglomerate) was removed from the statistical calculation for the subunit.

^aDepth denotes the measured depth but is almost equal to the true vertical depth because the deviation angle of FDB-1 was <1°.

borehole wall. Overall, the SN and LN resistivities showed similar patterns of change with depth throughout the entire logged depth range (Figure 11g). For example, the resistivity values were higher in massive lava bodies and hard andesite boulders in sedimentary rocks and lower in sedimentary formations.

The LN resistivity showed low values of ~30–50 Ω-m in the sedimentary rocks of Units III (siltstone and sandstone) and VI (conglomerate and tuffaceous conglomerate; Figure 11g and Table 2). The resistivity in Unit V (Pre-Aso volcanic rocks) increased gradually from ~60 to ~450 Ω-m with increasing depths from the unit boundary between IV and V to the middle part of the massive andesite (subunit Vb), maintained a high value for an ~50 m interval, and then decreased to ~200 Ω-m around the subunit boundary between Vb and Vc. The resistivity in subunit Vc varied within ~50–300 Ω-m and revealed lower values in the zones containing brown clay in the vicinity of Fault 461.

The long normal resistivity at Fault 354, which is the boundary between subunits IVb and Va, showed the lowest value of ~60 Ω-m but increased to ~460 Ω-m downward within a short (~20 m) interval. Downward to the second Fault 461 located a few meters below the subunit boundary between Vb and Vc, the resistivity rapidly decreased from ~490 Ω-m to the minimum value of ~150 Ω-m in an ~15 m interval (~447–462 m). However, at Fault 576, no clear resistivity change was observed (Figure 11g).

5.4. P-Wave Velocity

Overall, the P-wave velocity in FDB-1 tended to change depending on the lithofacies and textural features of the rocks and correlated with the resistivity. In comparison, the P-wave velocity appeared to indicate a better correlation with lithological units/subunits than the resistivity (Figures 11g and 11h). In other words, the velocity revealed similar values in individual subunits, except in subunit Vb, but clearly changed around unit/subunit boundaries. Specifically, the P-wave velocity showed values of ~1.8–2.1 km/s in the sedimentary formations of siltstone/sandstone (Unit III) and lapilli tuff (subunit IVa) and ~2.7–2.8 km/s in conglomerates of subunit IVb and autobrecciated lava of subunit Va, although several spike-shaped positive peaks (i.e., suddenly increased by ~1 km/s or more) were found in the sheet lava of subunit Va. Typically, the P-wave velocity in the massive lava of subunit Vb revealed the highest velocity values in the whole FDB-1 borehole in the range of ~4–5 km/s but decreased to ~3 km/s in a zone with high fracture density (discussed in the next section) at a depth of ~425 m. The velocity of subunit Vc indicated an average value of ~2.7 km/s, which was substantially lower than that of subunit Vb and almost the same as that of subunit Va. Overall, the P-wave velocity in Unit VI consisting of sedimentary rocks revealed similar values of ~2.7 km/s in the ~150 m-thick depth interval. The tuffaceous conglomerate (subunit VIb) showed a more stable velocity than the other units/subunits and revealed a downward velocity that gradually increased to the borehole bottom. In addition, the velocity varied locally and significantly at some

depths, showing, for example, a higher value of ~ 3.8 km/s for an andesite boulder (~ 553 m) and lower values of ~ 2.0 km/s for thin layers of siltstone and sandstone (~ 560 and ~ 532 m, respectively).

The P-wave velocity variations around the three damage zones showed features similar to those of resistivity (Figures 11g and 11h). At the shallowest damage zone, that is, Fault 354, which is the boundary between subunits IVb and Va, the P-wave velocity decreased locally and distinctly, reaching the lowest value (~ 1.7 km/s). At Fault 461, the P-wave velocity significantly and gradually decreased from ~ 4.5 to ~ 2.5 km/s within a narrow depth range (from ~ 451 to ~ 461 m) immediately above the fault and then showed an almost constant value in the footwall of the fault. In addition, at Fault 576, no clear change was observed, but in a detailed view, a small positive peak was observed in the velocity-depth profile.

5.5. Fracture Density and Attitude

The fracture density was determined by counting a total of 910 fractures in the FDB-1 cores at depths from ~ 302 to ~ 666 m (Figure 11i). In addition, angles of dip of all the fractures were recorded and categorized as “L,” meaning less than 30° from the horizontal plane, “M” for angles $\geq 30^\circ$ and $< 60^\circ$, and “H” for angles $\geq 60^\circ$. The results of counting fracture numbers indicated that the fractures were concentrated in Unit V of the Pre-Aso volcanic rocks. In general, fractures are more easily identified in brittle rocks, such as massive andesite, than in autobrecciated lavas and conglomerates (see Figure 7). On the other hand, the weakening of the andesitic matrix in the autobrecciated lava and conglomerate and/or loose contacts between gravel and matrix might scarcely be evaluated by fracture counting. Such structures, however, probably result in rock that is mechanically weak (i.e., low P-wave velocity, low resistivity, and possibly low Young's modulus and compressive strength).

The fracture density in subunit Va was < 5 fractures/m, excluding the area around Fault 354, and there were some intervals where the fracture density in subunits Vb and Vc was greater than 5 fractures/m. Low-angle fractures (shown in blue in Figure 11i) were dominant in the upper and lower parts of the thick massive lava (subunit Vb), where the fracture density was clearly higher than that in other parts of the borehole. The maximum fracture density in the upper part of subunit Vb (~ 390 – 400 m) reached 25 fractures/m. These fractures probably made the borehole wall unstable and resulted in the failure of log tool installation there. At depths from ~ 400 m down to ~ 510 m (subunits Vb and Vc), the fracture density seemed to change periodically. Distinctively, in the depth range of 420–434 m, the fracture density showed high values of 5–15 fractures/m, and their attitudes had predominantly medium to high angles (M and H, shown as green and red in Figure 11i). In this densely fractured zone, the P-wave velocity revealed a clear negative peak. Three depth intervals of 443–457, 466–478, and 491–503 m in and around Fault 461 showed fracture densities greater than 5 fractures/m.

A clear borehole wall image obtained by BHTV in FDB-1, which was especially clear in andesite Unit V, enabled us to select fractures (Figure 6). In total, we counted 288 fractures, including 38 clear fractures and 250 slightly unclear fractures (refer to Figure 6). We measured the fracture angles of dip (using the same three categories L, M, and H as the fracture records observed in rock cores) and their dip azimuths through BHTV images (Figure 11j). The fracture numbers of categories L, M, and H were 40, 176, and 72, respectively, showing that fractures with medium and high angles were dominant in the FDB-1 borehole. The dip azimuths of the M and H fractures were dominantly distributed from northwest to northeast (approximately 315 – 45°). Therefore, their strikes were dominantly distributed between the northeast-southwest (NE-SW) and northwest-southeast (NW-SE) directions. This observation revealed that the fracture strikes did not concentrate in a coherent direction but ranged widely from subparallel to orthogonal to approximately NE-SW with respect to the surface rupture of the Futagawa fault that formed during the 2016 Kumamoto earthquake mainshock.

6. Discussion

6.1. A Large Cumulative Normal Faulting Displacement on the Currently Dextral Strike-Slip Futagawa Fault

Three boreholes drilled into the currently dextral strike-slip Futagawa fault in southwestern Japan revealed a significant component of normal-sense motion in the past (Figures 4 and 8). From the core samples retrieved from the deviated borehole FDP-1, the true depth of the boundary between the Shimojin Gravel and Tsumori Formations was exactly identified at 87 m (see a core picture of Units II and III shown in Figure 7). This true

depth in FDP-1 corresponds to 86 m in the FDB borehole because the ground surface at FDP-1 is 1.3 m higher than that at FDB. FDP-1 penetrated ~ 26 m (vertical thickness) of the Tsumori Formation but did not reach the bottom. In borehole FDB-1, the depth of the boundary between the Shimojin Gravel and Tsumori Formations was approximately identified by cutting samples at a depth of ~ 291 m with an uncertainty of <10 m, which is the sampling interval of cutting. Coring began at a depth of 302 m in FDB-1; consequently, the exact bottom depth of the Tsumori Formation was identified as 317 m, and the thickness of the formation was suggested to be ~ 26 m, consistent with the thickness estimated in FDP-1. Most importantly, an ~ 205 m cumulative displacement in the vertical direction caused by normal faulting was determined from the difference between the depth of the boundary between the Shimojin Gravel and Tsumori Formations at FDP-1 and FDB-1. This large offset of the Futagawa fault zone with cumulative displacement in a normal faulting regime was first found in this drilling project. Assuming that the fault dips at 77° , as estimated by directly connecting the surface rupture and the depth of Fault 354 with the dip-slip faulting sense (Figure 4), the cumulative normal faulting displacement along the fault plane can be estimated as ~ 210 m. Even considering the uncertainty in the depth identified by cuttings in FDB-1, the dip of the fault, and a possible decrease in the thickness of the sedimentary formations at FDB-1 due to the larger overburden pressure present compared with that at FDP-1, the cumulative normal faulting displacements along the fault plane obviously reached more than 200 m. This large normal faulting displacement consists of the offset on the southeastern side of the Kiyama-Kashima graben (Figures 2a and 3).

The Futagawa fault was first investigated and defined according to an ~ 70 – 100 m dip-slip offset observed in Takayubaru lava (~ 9 km wide in the west-east direction, ~ 4 km in the north-south direction, and ~ 70 – 80 m in thickness), which is distributed ~ 1 km north or northeast of the FFDP site and formed 90 ± 4 ka (Matsumoto, 1996; Watanabe & Ono, 1969). This offset, however, was not observed in the slightly younger Aso-4 pyroclastic flow deposit (87 ka; e.g., Kumamoto Prefecture, 1996). This discrepancy suggests that the normal faulting activity on the Futagawa fault ceased before or around 87 ka. On the other hand, the age of the Shimojin Gravel and Tsumori Formations near their boundary showing the >200 m offset confirmed in this study is ~ 400 ka (Hase & Iwauchi, 1992). This suggests that the cumulative offset cutting the formation boundary formed later than ~ 400 ka. Therefore, the period for accumulating the >200 m displacement can be generally estimated as <300 k.y.; giving an average rate for normal faulting displacement of >0.7 m/k.y.

The Futagawa fault ruptured by dextral strike-slip motion during the 2016 Kumamoto earthquake mainshock, which might suggest a considerable difference between the paleotectonic stress environment that caused normal faulting and the current tectonic stress state. Oohashi et al. (2020) concluded that the Futagawa fault zone showed multistage deformation throughout the Neogene-Quaternary from normal faulting to dextral faulting, reflecting significant changes in the tectonic stress state. Our observations of the large cumulative normal faulting displacement are consistent with the interpretation by Oohashi et al. (2020).

At the junction of the Southwest Japan arc and Ryukyu arc, subduction of the Philippine Sea plate with fluid-rich materials introduced large volumes of fluids into the active arc system, leading to voluminous volcanism and a locally extensional stress regime (Aizawa et al., 2021; Mahony et al., 2011). As a result, in the Aso volcanic region, four large caldera-forming eruptions (Aso-1–Aso-4) occurred from ~ 300 to ~ 87 ka, and the large caldera was formed by losing large amounts of magma beneath the volcanic region. During the formation of the Aso caldera, the intensity of compression caused by plate convergence might have decreased, and an extensional stress regime might have become dominant in the Aso volcanic region. However, after termination of the large caldera-forming eruption sequence, the tectonics gradually changed from a transtensional (dominant extension) environment to the current transtensional (dominant strike-slip) environment by subduction of the Philippine Sea plate beneath the Kyushu Island (Figure 1a). Although transpressional and compressive environments are generally formed in subduction zones, nonuniform tectonic stress environments exist in Kyushu area, that is, normal, strike-slip, and reverse faulting regimes were formed in northern, central, and southern Kyushu, respectively (Yoshida, 2017). Strike-slip-dominant transtension was formed at the junction of the oblique plate subduction in the Nankai Trough and the normal plate subduction in the Ryukyu Trench (Figure 1a) because of the unique geometry of the plate interfaces, which protruded northwest and possibly resulted in an abnormal stress field (Figure 1a). In addition, the depth of the boundary between the subducting and overriding plates directly below the Aso volcanic region reaches approximately 100 km, and its dip is steeper than that at shallower depths (Ide et al., 2010). These factors may also make the stress field at the rupturing depths of the Futagawa fault more complicated and may have produced a transtensional stress field. This currently transtensional (dominant strike-slip) environments

is compatible with a previous study by Toda et al. (2016), who suggested slip partitioning of strike-slip on the Futagawa fault and dip-slip on the Idenokuchi fault during the 2016 Kumamoto earthquake mainshock. Therefore, we interpret that the change in faulting patterns of the Futagawa fault was caused by termination of the Aso caldera-forming eruption sequence. This finding may suggest that a seismogenic fault situated within an active volcanic field in an active arc can change its activities induced by magmatic processes and plate movements.

Trench parallel strike-slip fault systems can be formed by plate movements in plate convergence zones, including oblique subduction zones (e.g., Chemenda et al., 2000; Fitch, 1972). The slip motion of a fault is known to change as a result of the direction change of plate movement, which is the driving force behind fault activity (e.g., Antolín et al., 2012). The history of fault motion is quantitatively clarified by geochronological data combined with field observations (e.g., Cooper et al., 2015; Kubota et al., 2020). The inversion of slip-sense along the Doruneh fault from dextral to sinistral strike-slip occurred due to a diminishing anticlockwise rotation of the central Iranian Microplate (Javadi et al., 2013). The Yadong cross structure in the Himalayas was documented to have accommodated both normal-slip and strike-slip motions (e.g., Antolín et al., 2012; Cooper et al., 2012; Drukpa et al., 2006; Kellett & Grujic, 2012). The intraarc, trench-parallel Domeyko fault system in the Andes comprises strike-slip faults that have accommodated oblique plate convergence. Over time, this system has switched between dextral and sinistral strike-slip motions and accommodated normal-sense motion on the order of several hundred meters (e.g., McInnes et al., 1999; Reutter et al., 1996). McInnes et al. (1999) revealed ancient vertical displacements of at least 600 m along a major strike-slip West fault in northern Chile based on geochronological data. The Futagawa fault, the target of this study, is considered to have had strike-slip fault motion during its long history, and this study suggests that the Futagawa fault had cumulative >200 m of normal-faulting motion in a short period between ~300 and ~87 ka. The vertical displacement >200 m along the Futagawa fault is not the largest in the world, but we consider that this quantitative displacement is large enough to reveal that an ancient cumulative normal faulting displacement occurred exactly along the current strike-slip fault related to volcanic activities.

6.2. Geological and Geophysical Comparisons Among the Three Faults

In the cored depth intervals in the FDB-1 borehole, three main damage zones with high angles (approximately 60–80°) were observed (see Figures 8 and 9). Fault 354 is located at the boundary between lithological units IV (conglomerate) and V (andesite); Fault 461 is very close to the boundary between subunits Vb (massive andesite) and Vc (autobrecciated andesite); in detail, the depths of the center (fault core) and the top of its fractured zone are ~3.6 and ~1.2 m below the boundary, respectively, but Fault 576 is contained within subunit VIb (tuffaceous conglomerate). The damage zone at Fault 461, including the fault core, breccia, and fractured zone, is wider (~45 m in vertical thickness) than those of the other two damage zones (~3–6 m in vertical thickness), and more strongly damaged than the others as suggested by P-wave velocity and resistivity changes observed in log data. In addition, a large amount of brown clay was confirmed mainly in the high fracture density intervals of Fault 461 but is not found in the others. Additional important features confirmed are that slickenlines with a strike-slip faulting sense were observed on Fault 461 (Figures 10b–10e), that dip-slip faulting slickenlines were observed on Fault 354 (Figure 10a) but that no clear slickenlines were observed on Fault 576.

Changes in the physical properties with depth determined by downhole logging revealed different patterns in the vicinities of the three damage zones (Figure 11). At Fault 354, both resistivity and P-wave velocity measurements showed negative peaks. In the case of Fault 461, both the resistivity and P-wave velocity showed gradual but rapid and significant decreases from ~451 m toward the fault core at ~461 m, and the lowest values were attained there. For example, the P-wave velocity decreased from ~4.5 to ~2.5 km/s at Fault 461 but from ~2.7 to ~1.7 km/s at Fault 354 (Figure 11h). However, no clear reductions in the resistivity and P-wave velocity were observed at Fault 576, although the resistivity and velocity showed relatively lower values there.

On the basis of core descriptions in the FDB-1 borehole, we prefer to consider the depth range from ~353 to ~577 m as the whole deformation zone of the Futagawa fault, which has undergone all the old and recent fault motions, including both strike-slip and normal faulting. In Unit V (the volcanic rocks), abundant fractures, including minor faults, were observed in both cores and borehole images (Figures 11i and 11j). Among them, fractures with middle ($\geq 30^\circ$) and high ($\geq 60^\circ$) angles of dip might have formed related to the faulting activity of the Futagawa fault. Fractures/minor faults both accompanied by brown clay and without clay were observed. Around the fractures/minor faults with clay, resistivity clearly decreased, and spontaneous potential increased; several strike-slip faulting slickenline structures were observed in the clay-rich areas within the damage zone of

Fault 461 (Figures 10b–10e). Because substantial clays that filled the fractures/minor faults looked semiconsolidated and tightly bonded with the surrounding andesite, such fractures/minor faults were possibly formed during previous faulting activity but not in the recent 2016 Kumamoto earthquake mainshock. The three slip planes at approximately 460.5 m cut across the clay fill structures and therefore were considered relatively newly ruptured slip zones.

6.3. Correlation Between the Borehole Observations and the 2016 Kumamoto Earthquake

To definitively penetrate the slip zone ruptured during the 2016 Kumamoto earthquake mainshock, the FFDP was conducted close to the surface rupture, and three boreholes penetrated the fault at different depths (Figures 2 and 4). On the ground surface around the drilling site, a single coseismic rupture was formed. However, multiple faults discussed above were confirmed in the depth range of 353–577 m in FDB-1, corresponding to an ~55 m-thick zone perpendicular to the fault plane, which could be considered to have formed by repeated faulting activity. As the records of fault rupturing were investigated through trench excavations across the Futagawa fault surface rupture including one site near FFDP site, multiple historic events were confirmed in the past ~10,000 years (e.g., Toda et al., 2019). Most likely, such repeated fault rupturing formed multiple fault planes and expanded throughout the whole fault zone thickness (e.g., Choi et al., 2016; Faulkner et al., 2003).

From the comparisons among the three main damage zones running through FDB-1, some slickenlines indicating strike-slip motions were observed in Fault 461. In addition, this damage zone revealed the most significant resistivity, and the P-wave velocity decreased immediately above the damage zone. Therefore, we suggest that Fault 461 may be the primary candidate for the seismogenic fault of the 2016 Kumamoto earthquake mainshock. As dip-slip faulting slickenlines were observed on the slip plane at 354 m, some normal faulting events possibly occurred on this plane. Due to a dramatic tectonic stress environment change ~87 ka, the rupture mechanism changed from dominant normal faulting to strike-slip faulting. As a result, the rupture activity also changed locations (slip zones); as an example, in the case of the FFDP site, it appeared to have changed from Fault 354 to Fault 461.

Assuming that Fault 461 in FDB-1 ruptured during the 2016 Kumamoto earthquake mainshock, subunit Vb (massive andesite) in the hanging wall has higher P-wave velocity and therefore higher elastic Young's modulus than subunits Vc, VIa, and VIb in the footwall. Differences in the geological structures and geophysical properties of the hanging wall and footwall of the ruptured fault plane might possibly affect stress and strain accumulation mechanisms in interseismic periods and result in different coseismic ground motions as well as damage to buildings caused by motions on the hanging wall side (northwestern side of the surface rupture) and on the footwall side, as reported by Murase et al. (2018).

7. Conclusion

To reproduce ancient and current rupturing patterns of the Futagawa fault zone and to reveal geological characteristics and physical properties in and around the fault zone that dextrally ruptured during the 2016 Kumamoto earthquake mainshock in Japan, we summarized the results of the FFDP preliminarily reported by Kyoto University (2018). In addition, we reanalyzed core descriptions and downhole logging data and newly counted fracture data from both core samples and log images. Consequently, the conclusions obtained in this study are as follows:

1. The core samples retrieved from boreholes FDP-1 and FDB-1 drilled through the Futagawa fault along the same transect orthogonal to the surface rupture that formed during the mainshock revealed a large cumulative normal faulting displacement (>200 m) along the Futagawa fault. Combining this information with previous geological studies, the cumulative normal faulting displacement can be considered to have formed by Futagawa fault activity before ~87 ka within an ~300 k.y. period (Middle-Late Pleistocene). After ~87 ka, however, the active fault dominantly ruptured in a strike-slip regime similar to that of the 2016 Kumamoto earthquake mainshock. We interpret the termination of the Aso caldera-forming eruption sequence in which the last eruption was Aso-4 as causing a significant change in the tectonic stress state that governed the faulting regime. This interpretation suggests that a seismogenic fault in an active volcanic region in an active arc can change its activities induced by magmatic processes and plate movements. The observations in this study from the Aso volcanic region in the Japan island arc should apply more broadly to similar volcanic arcs at subduction zones.

2. In borehole FDB-1, three damage zones with sharp slip plane(s) were penetrated at depths of approximately 354 m, 461 m, and 576 m. At Fault 461, the damage zone is wider and more strongly disturbed than those of the others, and much brown clay was confirmed within the damage zone of Fault 461 but is not found near the others. Additional important features confirmed are that some slickenlines of strike-slip faulting were observed on Fault 461, that dip-slip faulting slickenlines were observed on Fault 354 but that no clear slickenline was seen on Fault 576.

The depth profiles of physical properties obtained by downhole logging reveal different patterns of change in and around the three damage zones. At Fault 461, both resistivity and P-wave velocity show gradual but rapid and significant changes from ~451 m toward the fault core at ~461 m and attain the lowest values there. For example, the P-wave velocity decreases from ~4.5 km/s to ~2.5 km/s.

3. On the basis of the investigated geological characteristics and geophysical property distributions, we suggest that the damage/slip zone at 461 m may represent the primary candidate for the seismogenic fault of the 2016 Kumamoto earthquake mainshock. Assuming that Fault 461 ruptured during the mainshock, lithological sub-unit Vb (massive andesite) in the hanging wall has higher P-wave velocity and therefore higher elastic Young's modulus than those of subunits Vc, VIa, and VIb in the footwall. The differences in the lithological structures and geophysical properties between the hanging wall and footwall of the ruptured fault in 2016 might be related to the fact that coseismic ground motion characteristics differed on the hanging wall side (northwestern side of the surface rupture) and on the footwall side during the 2016 earthquake mainshock.

Data Availability Statement

All the geophysical logging data and fracture density from core description and fracture attitudes determined from the borehole images are available on the Pangaea data publisher for earth and environmental science (<https://doi.pangaea.de/10.1594/PANGAEA.933472>). All information of the detailed drilling and logging operation was reported in a technical report (in Japanese) available on the website of Nuclear Regulation Authority, Japan (<https://www.nsr.go.jp/data/000256426.pdf>).

Acknowledgments

The authors sincerely thank Katsushi Tanoue for permitting to drill multi-boreholes in his farmland, and all the members of the Kyoto University team and Masahiro Miyawaki for conducting the Futagawa fault drilling project in which the raw data used in this study was obtained. Constructive comments from Frances Cooper and an anonymous reviewer were very helpful for improving the manuscript. The authors gratefully acknowledge Nana Kamiya for providing a core photo used in Figures 10c and 10d; and Yoshiki Shirahama for providing his editable map used in Figures 1a and 2a in this paper. The Futagawa fault drilling project conducted by Kyoto University was supported by consignment expenses of the Nuclear Regulation Authority, Japan. Part of the works was supported by Grants-in-Aid for Scientific Research 19H00717 of the Japan Society for the Promotion of Science (JSPS), Japan.

References

- Aizawa, K., Takakura, S., Asaue, H., Koike, K., Yoshimura, R., & Yamazaki, K. (2021). Electrical conductive fluid-rich zones and their influence on the earthquake initiation, growth, and arrest processes: Observations from the 2016 Kumamoto earthquake sequence, Kyushu Island, Japan. *Earth Planets and Space*, 73(1), 12. <https://doi.org/10.1186/s40623-020-01340-w>
- Albert, P. G., Smith, V. C., Suzuki, T., McLean, D., Tomlinson, E. L., Miyabuchi, Y., et al. (2019). Geochemical characterisation of the Late Quaternary widespread Japanese tephrostratigraphic markers and correlations to the Lake Suigetsu sedimentary archive (SG06 core). *Quaternary Geochronology*, 52, 103–131. <https://doi.org/10.1016/j.quageo.2019.01.005>
- Ando, M. (2001). Geological and geophysical studies of the Nojima Fault from drilling: An outline of the Nojima Fault Zone Probe. *Island Arc*, 10(3–4), 206–214. <https://doi.org/10.1111/j.1440-1738.2001.00349.x>
- Antolín, B., Schill, E., Grujic, D., Baule, S., Quidelleur, X., Appel, E., et al. (2012). E–W extension and block rotation of the southeastern Tibet: Unravelling late deformation stages in the eastern Himalayas (NW Bhutan) by means of pyrrhotite remanences. *Journal of Structural Geology*, 42, 19–33. <https://doi.org/10.1016/j.jsg.2012.07.003>
- Aoki, K. (2008). Revised age and distribution of ca. 87 ka Aso-4 tephra based on new evidence from the northwest Pacific Ocean. *Quaternary International*, 178(1), 100–118. <https://doi.org/10.1016/j.quaint.2007.02.005>
- Chemenda, A., Lallemand, S., & Bokun, A. (2000). Strain partitioning and interplate friction in oblique subduction zones: Constraints provided by experimental modeling. *Journal of Geophysical Research: Solid Earth*, 105(B3), 5567–5581. <https://doi.org/10.1029/1999JB00332>
- Choi, J. H., Edwards, P., Ko, K., & Kim, Y. S. (2016). Definition and classification of fault damage zones: A review and a new methodological approach. *Earth-Science Reviews*, 152, 70–87. <https://doi.org/10.1016/j.earscirev.2015.11.006>
- Cooper, F. J., Adams, B. A., Edwards, C. S., & Hodges, K. V. (2012). Large normal-sense displacement on the South Tibetan fault system in the eastern Himalaya. *Geology*, 40(11), 971–974. <https://doi.org/10.1130/G33318.1>
- Cooper, F. J., Hodges, K. V., Parrish, R. R., Roberts, N. M. W., & Horstwood, M. S. A. (2015). Synchronous N-S and E-W extension at the Tibet-to-Himalaya transition in NW Bhutan. *Tectonics*, 34(7), 1375–1395. <https://doi.org/10.1002/2014TC003712>
- DeMets, C., Gordon, R. G., & Argus, D. F. (2010). Geologically current plate motions. *Geophysical Journal International*, 181(1), 1–80. <https://doi.org/10.1111/j.1365-246X.2009.04491.x>
- Doan, M.-L., Conin, M., Henry, P., Wiersberg, T., Boutt, D., Buchs, D., et al. (2011). Quantification of free gas in the Kumano fore-arc basin detected from borehole physical properties: IODP NanTroSEIZE drilling site C0009. *Geochemistry, Geophysics, Geosystems*, 12, Q0AD06. <https://doi.org/10.1029/2010GC003284>
- Drukpa, D., Velasco, A. A., & Doser, D. I. (2006). Seismicity in the Kingdom of Bhutan (1937–2003): Evidence for crustal transcurrent deformation. *Journal of Geophysical Research: Solid Earth*, 111(B6), B06301. <https://doi.org/10.1029/2004JB003087>
- Faulkner, D. R., Lewis, A. C., & Rutter, E. H. (2003). On the internal structure and mechanics of large strike-slip fault zones: Field observations of the Carboneras fault in southeastern Spain. *Tectonophysics*, 367(3–4), 235–251. [https://doi.org/10.1016/S0040-1951\(03\)00134-3](https://doi.org/10.1016/S0040-1951(03)00134-3)
- Feuillet, N. (2013). The 2011–2012 unrest at Santorini rift: Stress interaction between active faulting and volcanism. *Geophysical Research Letters*, 40(14), 3532–3537. <https://doi.org/10.1002/grl.50516>

- Fitch, T. J. (1972). Plate convergence, transcurrent faults, and internal deformation adjacent to southeast Asia and the western Pacific. *Journal of Geophysical Research*, 77(23), 4432–4460. <https://doi.org/10.1029/JB077i023p04432>
- Fulton, P. M., Brodsky, E. E., Kano, Y., Mori, J., Chester, F., Ishikawa, T., et al. (2013). Low coseismic friction on the Tohoku-Oki fault determined from temperature measurements. *Science*, 342(6163), 1214–1217. <https://doi.org/10.1126/science.1243641>
- Furukawa, K., Miyoshi, M., Shimura, T., Shibata, T., & Arakawa, Y. (2009). Geology and petrology of the pre-Aso volcanic rocks distributed in the NW wall of Aso caldera: Eruption style and magma plumbing system of the pre-caldera volcanism. *The Journal of the Geological Society of Japan*, 115(12), 658–671. (in Japanese with English abstract). <https://doi.org/10.5575/geosoc.115.658>
- Geospatial Information Authority of Japan. (2017). *5-m-mesh digital elevation model (DEM) and basic items of the fundamental geographic data*. Retrieved from <https://fgd.gsi.go.jp/download/menu.php>
- Geospatial Information Authority of Japan. (2020). *5-m-mesh digital elevation model (DEM) of the fundamental geographic data*. Retrieved from <https://fgd.gsi.go.jp/download/menu.php>
- Goldberg, D. (1997). The role of downhole measurements in marine geology and geophysics. *Reviews of Geophysics*, 35, 315–342. <https://doi.org/10.1029/97RG00221>
- Hase, Y., & Iwauchi, A. (1992). *Correlation of Late Cenozoic system with Lacustrine Deposits in central Kyushu - Kumamoto and Oita area* (Vol. 27, pp. 69–95). Memoirs of the Faculty of General Education, Kumamoto University, Natural Sciences, Geology. (in Japanese with English abstract).
- Hase, Y., & Iwauchi, A. (1993). Displacement of the depressed areas in the graben, estimated by the altitude of the inland sediments in central Kyushu, Japan. *Memoirs of the Geological Society of Japan*, 41, 53–72. (in Japanese with English abstract). https://dl.ndl.go.jp/view/download/digidepo_10810076_po_ART0003485304.pdf?contentNo=1&alternativeNo=
- Hayashi, M., Yahiro, K., Kitamura, N., & Kitabayashi, E. (2004). Middle Pleistocene fossil insects from the Tsumori Formation of Mashiki-machi, Kumamoto Prefecture, Japan (Part 2). *Bulletin of the Mizunami Fossil Museum*, 31, 63–67. (in Japanese with English abstract). https://www.city.mizunami.lg.jp/_res/projects/default_project/_page_001/002/297/2014092922957_hayashi1.pdf
- Hoshizumi, H., Ozaki, M., Miyazaki, K., Matsuura, H., Toshimitsu, S., Uto, K., et al. (2004). *Geological map of Japan 1:200,000, Kumamoto* (in Japanese). Geological Survey of Japan, AIST. Retrieved from https://www.gsj.jp/data/200KGM/PDF/GSJ_MAP_G200_NI5211_2004_D.pdf
- Hosono, T., Hartmann, J., Louvat, P., Amann, T., Washington, K. E., West, A. J., et al. (2018). Earthquake-induced structural deformations enhance long-term solute fluxes from active volcanic systems. *Scientific Reports*, 8(1), 14809. <https://doi.org/10.1038/s41598-018-32735-1>
- Hosono, T., Yamada, C., Manga, M., Wang, C. Y., & Tanimizu, M. (2020). Stable isotopes show that earthquakes enhance permeability and release water from mountains. *Nature Communications*, 11, 2776. <https://doi.org/10.1038/s41467-020-16604-y>
- Hosono, T., Yamada, C., Shibata, T., Tawara, Y., Wang, C. Y., Manga, M., et al. (2019). Coseismic groundwater drawdown along crustal ruptures during the 2016 Mw 7.0 Kumamoto earthquake. *Water Resources Research*, 55(7), 5891–5903. <https://doi.org/10.1029/2019WR024871>
- Ide, S., Shiomi, K., Mochizuki, K., Tonegawa, T., & Kimura, G. (2010). Split Philippine Sea plate beneath Japan. *Geophysical Research Letters*, 37(21), L21304. <https://doi.org/10.1029/2010GL044585>
- Ikeda, R. (2001). Outline of the fault zone drilling project by NIED in the vicinity of the 1995 Hyogo-ken Nanbu earthquake, Japan. *Island Arc*, 10(3–4), 199–205. <https://doi.org/10.1111/j.1440-1738.2001.00318.x>
- Imanishi, S. (1967). Trapa remains from the Tsumori Formation, Kumamoto Prefecture, central Kyushu. *Kumamoto Journal of Science, Series B, Section 1*, 7(1), 1–8.
- Ishizaka, S., Watanabe, K., & Takada, H. (1992). Subsidence rate of the underground Quaternary system for the past 150,000 years in the Kumamoto Plain, Kyushu, Japan. *The Quaternary Research*, 31, 91–99. (in Japanese with English abstract). <https://doi.org/10.4116/jaqua.31.91>
- Javadi, H. R., Ghassemi, M. R., Shahpasandzadeh, M., Guest, B., Ashtiani, M. E., Yassaghi, A., et al. (2013). History of faulting on the Doruneh Fault System: Implications for the kinematic changes of the Central Iranian Microplate. *Geological Magazine*, 150(4), 651–672. <https://doi.org/10.1017/S0016756812000751>
- Kamata, H., & Kodama, K. (1999). Volcanic history and tectonics of the Southwest Japan Arc. *Island Arc*, 8(3), 393–403. <https://doi.org/10.1046/j.1440-1738.1999.00241.x>
- Kaneoka, I., & Suzuki, M. (1970). K-Ar and fission track ages of some obsidians from Japan. *The Journal of the Geological Society of Japan*, 76(6), 309–313. <https://doi.org/10.5575/geosoc.76.309>
- Kellett, D. A., & Grujic, D. (2012). New insight into the South Tibetan detachment system: Not a single progressive deformation. *Tectonics*, 31(2), TC2007. <https://doi.org/10.1029/2011TC002957>
- Kobayashi, H., Koketsu, K., & Miyake, H. (2017). Rupture processes of the 2016 Kumamoto earthquake sequence: Causes for extreme ground motions. *Geophysical Research Letters*, 44(12), 6002–6010. <https://doi.org/10.1002/2017GL073857>
- Koike, K., Yoshinaga, T., & Asaue, H. (2009). Radon concentrations in soil gas, considering radioactive equilibrium conditions with application to estimating fault-zone geometry. *Environmental Geology*, 56(8), 1533–1549. <https://doi.org/10.1007/s00254-008-1252-x>
- Koike, K., Yoshinaga, T., Ueyama, T., & Asaue, H. (2014). Increased radon-222 in soil gas because of cumulative seismicity at active faults. *Earth, Planets and Space*, 66(57), 1–9. <https://doi.org/10.1186/1880-5981-66-57>
- Kubota, Y., Takeshita, T., Yagi, K., & Itaya, T. (2020). Kinematic analyses and radiometric dating of the large-scale Paleogene two-phase faulting along the median tectonic line, Southwest Japan. *Tectonics*, 39(2), e2018TC005372. <https://doi.org/10.1029/2018TC005372>
- Kumamoto Prefecture. (1996). FY1995 researches on the Futagawa and Tatedayama faults. *Report of grant-in-aid for earthquake research* (in Japanese). Retrieved from <https://www.hp1039.jishin.go.jp/danso/Kumamoto2Afrm.htm>
- Kusumoto, S. (2016). Dip distribution of Oita–Kumamoto Tectonic Line located in central Kyushu, Japan, estimated by eigenvectors of gravity gradient tensor. *Earth, Planets and Space*, 68(1), 153. <https://doi.org/10.1186/s40623-016-0529-7>
- Kyoto University. (2018). FY2017 commissioned for the disaster prevention on nuclear facilities (boring core and stress measurement using borehole: No.2 Futagawa Fault). *Technical Report* (in Japanese, Vol. 3/3, p. 208). Retrieved from <https://www.nsr.go.jp/data/000256426.pdf>
- Li, H., Wang, H., Xu, Z., Si, J., Pei, J., Li, T., et al. (2013). Characteristics of the fault-related rocks, fault zones and the principal slip zone in the Wenchuan Earthquake Fault Scientific Drilling Project Hole-1 (WFSD-1). *Tectonophysics*, 584, 23–42. <https://doi.org/10.1016/j.tecto.2012.08.021>
- Li, H., Xu, Z., Niu, Y., Kong, G., Huang, Y., Wang, H., et al. (2014). Structural and physical property characterization in the Wenchuan earthquake Fault Scientific Drilling project – hole 1 (WFSD-1). *Tectonophysics*, 619–620, 86–100. <https://doi.org/10.1016/j.tecto.2013.08.022>
- Li, H., Xue, L., Brodsky, E. E., Mori, J. J., Fulton, P. M., Wang, H., et al. (2015). Long-term temperature records following the Mw 7.9 Wenchuan (China) earthquake are consistent with low friction. *Geology*, 43(2), 163–166. <https://doi.org/10.1130/G35515.1>
- Lin, W., Byrne, T., Kinoshita, M., McNeill, L., Chang, C., Lewis, J., et al. (2016). Distribution of stress state in the Nankai subduction zone, southwest Japan and a comparison with Japan Trench. *Tectonophysics*, 692, 120–130. <https://doi.org/10.1016/j.tecto.2015.05.008>
- Lin, W., Conin, M., Moore, J. C., Chester, F. M., Nakamura, Y., Mori, J. J., et al. (2013). Stress state in the largest displacement area of the 2011 Tohoku-Oki earthquake. *Science*, 339(6120), 687–690. <https://doi.org/10.1126/science.1229379>

- Ma, K. F., Tanaka, H., Song, S. R., Wang, C. Y., Hung, J. H., Song, Y. F., et al. (2006). Slip zone and energetics of a large earthquake from the Taiwan Chelungpu-Fault Drilling Project. *Nature*, *444*(7118), 473–476. https://doi.org/10.5918/jamstecr.9.2_95
- Mahony, S. H., Wallace, L. M., Miyoshi, M., Villamor, P., Sparks, R. S. J., & Hasenaka, T. (2011). Volcano-tectonic interactions during rapid plate-boundary evolution in the Kyushu region, SW Japan. *Geological Society of America Bulletin*, *123*(11–12), 2201–2223. <https://doi.org/10.1130/B30408.1>
- Matsumoto, A. (1996). K-Ar age determinations of young volcanic rocks –correction for initial $^{40}\text{Ar}/^{36}\text{Ar}$ ratios and its application. *Chishitsu News*, *501*, 12–17. (in Japanese).
- Matsumoto, A., Uto, K., Ono, K., & Watanabe, K. (1991). K-Ar age determinations for Aso volcanic rocks –concordance with volcanostratigraphy and application to pyroclastic flows. *Paper B03 presented at 1991 Fall Meeting*. The Volcanological Society of Japan. https://doi.org/10.18940/vsj.1991.2.0_73
- McInnes, B. I. A., Farley, K. A., Sillitoe, R. H., & Kohn, B. P. (1999). Application of apatite (U-Th)/He thermochronometry to the determination of the sense and amount of vertical fault displacement at the Chuquicamata porphyry copper deposit, Chile. *Economic Geology*, *94*(6), 937–947. <https://doi.org/10.2113/gsecongeo.94.6.937>
- Moore, J. D. P., Yu, H., Tang, C. H., Wang, T., Barbot, S., Peng, D., et al. (2017). Imaging the distribution of transient viscosity after the 2016 Mw 7.1 Kumamoto earthquake. *Science*, *356*(6334), 163–167. <https://doi.org/10.1126/science.aal3422>
- Moya, L., Yamazaki, F., Liu, W., & Chiba, T. (2017). Calculation of coseismic displacement from LiDAR data in the 2016 Kumamoto, Japan, earthquake. *Natural Hazards and Earth System Sciences*, *17*(1), 143–156. <https://doi.org/10.5194/nhess-17-143-2017>
- Murase, S., Ohmura, S., Sugino, M., & Hayashi, Y. (2018). Relationship between characteristics of ground motions and ratio of collapsed wooden houses in the 2016 Kumamoto earthquake. *Journal of Japan Association for Earthquake Engineering*, *18*(2), 147–165. (in Japanese with English abstract). https://doi.org/10.5610/jaee.18.2_147
- Nakada, S., & Kamata, H. (1991). Temporal change in chemistry of magma source under central Kyushu, southwest Japan: Progressive contamination of mantle wedge. *Bulletin of Volcanology*, *53*, 182–194. <https://doi.org/10.1007/BF00301229>
- Nakata, T., & Imaizumi, T. (2002). *Digital active fault map of Japan* (p. 60). University of Tokyo Press. (in Japanese).
- Nakayama, H., Furusawa, W., Hase, Y., & Aramaki, S. (2019). *Geological cross sections of Kumamoto area—Subsurface geology and Kumamoto earthquake*. (p. 114). Kumamoto Jiban Kenkyukai. (in Japanese).
- Nishiwaki, T., & Lin, A. (2019). Fractures and subsidiary faults developed in the active strike-slip Nojima fault zone, Japan, and tectonic implications. *Tectonics*, *38*(12), 4290–4300. <https://doi.org/10.1029/2018tc005391>
- Oohashi, K., Otsubo, M., Matsumoto, S., Kobayashi, K., Sato, K., & Nishimura, T. (2020). The quaternary tectonics of central Kyushu and the 2016 Kumamoto earthquake: From a multifaceted viewpoint combining geology, seismology, and geodesy. *Journal of Geography*, *129*(4), 565–589. (in Japanese with English abstract). <https://doi.org/10.5026/jgeography.129.565>
- Oohashi, K., & Tamura, T. (2016). An outcrop of the active Futagawa Fault, which ruptured during the 2016 Kumamoto earthquake. *The Journal of the Geological Society of Japan*, *122*(12), V–VI. (in Japanese with English figure captions). <https://doi.org/10.5575/geosoc.2016.0055>
- Reutter, K. J., Scheuber, E., & Chong, G. (1996). The precordilleran fault system of Chuquicamata, northern Chile: Evidence for reversals along arc-parallel strike-slip faults. *Tectonophysics*, *259*(1–3), 213–228. [https://doi.org/10.1016/0040-1951\(95\)00109-3](https://doi.org/10.1016/0040-1951(95)00109-3)
- Sano, Y., Takahata, N., Kagoshima, T., Shibata, T., Onoue, T., & Zhao, D. (2016). Groundwater helium anomaly reflects strain change during the 2016 Kumamoto earthquake in Southwest Japan. *Scientific Reports*, *6*(1), 37939. <https://doi.org/10.1038/srep37939>
- Shirahama, Y., Yoshimi, M., Awata, Y., Maruyama, T., Azuma, T., Miyashita, Y., et al. (2016). Characteristics of the surface ruptures associated with the 2016 Kumamoto earthquake sequence, central Kyushu, Japan. *Earth, Planets and Space*, *68*(1), 191. <https://doi.org/10.1186/s40623-016-0559-1>
- Sutherland, R., Townend, J., Toy, V., Upton, P., Coussens, J., Allen, M., et al. (2017). Extreme hydrothermal conditions at an active plate-bounding fault. *Nature*, *546*, 137–140. <https://doi.org/10.1038/nature22355>
- Takarada, S., & Hoshizumi, H. (2020). Distribution and eruptive volume of Aso-4 pyroclastic density current and tephra fall deposits, Japan: A M8 super-eruption. *Frontiers in Earth Science*, *8*, 170. <https://doi.org/10.3389/feart.2020.00170>
- Tanaka, H., Nagumo, T., & Kashima, K. (2005). Fossil freshwater diatoms from Tsumori Formation (middle Pleistocene) in Mashiki town, Kumamoto Prefecture, Kyushu, Japan. *Diatom*, *21*, 119–130. (in Japanese with English abstract). https://doi.org/10.11464/diatom1985.21.0_119
- Tobin, H. J., Kimura, G., & Kodaira, S. (2019). Processes governing giant subduction earthquakes: IODP drilling to sample and instrument subduction zone megathrusts. *Oceanography*, *32*(1), 80–93. <https://doi.org/10.5670/oceanog.2019.125>
- Toda, S., Kaneda, H., Okada, S., Ishimura, D., & Mildon, K. Z. (2016). Slip-partitioned surface ruptures for the Mw 7.0 16 April 2016 Kumamoto, Japan, earthquake. *Earth, Planets and Space*, *68*(1), 188. <https://doi.org/10.1186/s40623-016-0560-8>
- Toda, S., Torii, M., Okuno, M., Konno, A., Ono, H., & Takahashi, N. (2019). Evidence for Holocene paleoseismic events on the 2016 Kumamoto earthquake rupture zone within the Aso caldera: A trench excavation survey at Kurokawa, the town of Minami-Aso, southwest Japan. *Active Fault Research*, *51*, 13–25. (in Japanese with English abstract). https://doi.org/10.11462/afr.2019.51_13
- Townend, J., Sutherland, R., Toy, V. G., Eccles, J. D., Boulton, C., Cox, S. C., & McNamara, D. (2013). Late-interseismic state of a continental plate-bounding fault: Petrophysical results from DFDP-1 wireline logging and core analysis, Alpine Fault, New Zealand. *Geochemistry, Geophysics, Geosystems*, *14*(9), 3801–3820. <https://doi.org/10.1002/ggge.20236>
- Tsuji, T., Ikeda, M., Furusawa, A., Nakamura, C., Ichikawa, K., Yanagida, M., et al. (2018). High resolution record of Quaternary explosive volcanism recorded in fluvio-lacustrine sediments of the Uwa basin, southwest Japan. *Quaternary International*, *471*, 278–297. <https://doi.org/10.1016/j.quaint.2017.10.016>
- Waite, G. P., & Smith, R. B. (2002). Seismic evidence for fluid migration accompanying subsidence of the Yellowstone caldera. *Journal of Geophysical Research*, *107*(B9), 2177. <https://doi.org/10.1029/2001JB000586>
- Watanabe, K., Momikura, Y., & Tsuruta, K. (1979). Active faults and parasitic eruption centers on the west flank of Aso caldera, Japan. *The Quaternary Research*, *18*(2), 89–101. (in Japanese with English abstract). <https://doi.org/10.4116/jaqua.18.89>
- Watanabe, K., & Ono, K. (1969). Geology of the vicinity of Omine on the western flank of the Aso caldera. *The Journal of the Geological Society of Japan*, *75*(7), 365–374. (in Japanese with English abstract). <https://doi.org/10.5575/geosoc.75.365>
- Wu, J., Suppe, J., Lu, R., & Kanda, R. (2016). Philippine Sea and East Asian plate tectonics since 52 Ma constrained by new subducted slab reconstruction methods. *Journal of Geophysical Research: Solid Earth*, *121*(6), 4670–4741. <https://doi.org/10.1002/2016jb012923>
- Yano, T. E., & Matsubara, M. (2017). Effect of newly refined hypocenter locations on the seismic activity recorded during the 2016 Kumamoto Earthquake sequence. *Earth, Planets and Space*, *69*(74), 1632. <https://doi.org/10.1186/s40623-017-0656-9>
- Yeh, E. C., Sone, H., Nakaya, T., Ian, K. H., Song, S. R., Hung, J. H., et al. (2007). Core description and characteristics of fault zones from hole-A of the Taiwan Chelungpu-Fault Drilling Project. *Terrestrial, Atmospheric and Oceanic Sciences*, *18*(2), 327–357. [https://doi.org/10.3319/TAO.2007.18.2.327\(TCDP\)](https://doi.org/10.3319/TAO.2007.18.2.327(TCDP))

- Yoshida, M. (2017). Re-evaluation of the regional tectonic stress fields and faulting regimes in central Kyushu, Japan, behind the 2016 Mw 7.0 Kumamoto Earthquake. *Tectonophysics*, 712–713, 95–100. <https://doi.org/10.1016/j.tecto.2017.05.011>
- Zhao, D., Yamashita, K., & Toyokuni, G. (2018). Tomography of the 2016 Kumamoto earthquake area and the Beppu-Shimabara graben. *Scientific Reports*, 8, 15488. <https://doi.org/10.1038/s41598-018-33805-0>
- Zoback, M., Hickman, S., Ellsworth, W., & The SAFOD Science Team. (2011). Scientific drilling into the San Andreas Fault Zone - An overview of SAFOD's first five years. *Scientific Drilling*, 11(1), 14–28. <https://doi.org/10.5194/sd-11-14-2011>
- Zoback, M., Hickman, S., & Ellsworth, W. (2007). The role of fault zone drilling. *Geophysics*, 4, 649–674. <https://doi.org/10.1016/B978-044452748-6.00084-5>